We are IntechOpen, the world's leading publisher of Open Access books
Built by scientists, for scientists

6,900
Open access books available

185,000
International authors and editors

200M
Downloads

154
Countries delivered to

Our authors are among the
TOP 1%
most cited scientists

12.2%
Contributors from top 500 universities

CLARIVATE ANALYTICS
BOOK CITATION INDEX
INDEXED

WEB OF SCIENCE™

Selection of our books indexed in the Book Citation Index
in Web of Science™ Core Collection (BKCI)

Interested in publishing with us?
Contact book.department@intechopen.com

Numbers displayed above are based on latest data collected.
For more information visit www.intechopen.com

Characterization of Sol-Gel-Derived and Crystallized HfO$_2$, ZrO$_2$, ZrO$_2$-Y$_2$O$_3$ Thin Films on Si(001) Wafers with High Dielectric Constant

Hirofumi Shimizu and Toshikazu Nishide

College of Engineering, Nihon University
Tamura-machi, Koriyama, Fukushima,
Japan

1. Introduction

A very great number of metal oxide thin films are produced by sol-gel methods. Metallic compounds dissolved in organic solvents are hydrolyzed and polymerized by adding H$_2$O with an acid or a base and heating to obtain metal oxide sols. Metal oxide thin films are prepared by coating the sols on substrates followed by firing (Kozuka, 2005).

The sol-gel method produces amorphous or crystalline thin gel films of metallic solid compounds by solidifying a sol formed by hydrolyzing and polymerizing a solution containing metallic compounds. Sol-gel processes are widely employed in the field of chemistry to prepare ceramic powders and thin films of hafnium oxide (HfO$_2$) (Nishide et al., 2000) and zirconium oxide (ZrO$_2$) (Liu et al., 2002) for obtaining high-quality ceramics and insulators, offering the advantages of low cost, relative simplicity, and easy control of the composition of the layers formed. This chapter describes the characterization of sol-gel-derived and crystallized HfO$_2$ and ZrO$_2$ thin films intended for use as gate insulators with high dielectric constants in electronic devices.

In the electronic device field, the continuing miniaturization of silicon (Si) ultra-large-scale-integration (ULSI) devices has required an ultrathin gate Si dioxide (SiO$_2$) and oxynitride film; upon scaling down to 32-22 nm technology nodes and beyond, thinner SiO$_2$ gate oxide films have been required. At these thicknesses, gate leakage currents due to direct tunneling become comparable to the off-currents of metal-oxide-semiconductor (MOS) field-effect transistors (FETs), increasing the off-state power consumption of the devices. In further scaled-down advanced Si complementary MOS (CMOS) devices, scaling trends have required the substitution of gate SiO$_2$ by insulators with higher dielectric constants (high-*k*) (Huff & Gilmer, 2004). The aim of using high-*k* materials is to increase the film thickness, thus reducing the tunneling leakage current, while scaling the capacitance of the equivalent oxide thickness (EOT) below the direct tunneling limit of SiO$_2$ (Huff & Gilmer, 2004). Several high-*k* material candidates, such as HfO$_2$ (Blanchin et al., 2008), ZrO$_2$ (Niinisto et al., 2004), Al$_2$O$_3$, ZrO$_2$-Y$_2$O$_3$ (YANG, 1996), Y$_2$O$_3$ (Nishide & Shibata, 2001), La$_2$O$_3$ (Ng et al., 2005), and gate stack structures have been proposed and some materials have been put into practical use. All of them are either oxides or silicates of 4d or 5d transition metals or rare earth elements.

HfO$_2$ and ZrO$_2$ thin films are the most promising candidates as alternative high permittivity (high-*k*) oxides for replacing the SiO$_2$ gate dielectric material used in CMOS devices (Gusev, 2005, Wilk et al., 2001). Because of the higher permittivity, the dielectric gate insulator thickness can be increased for a given capacitance, resulting in reduced tunneling leakage current. HfO$_2$ has promising properties such as high permittivity (25~40) (Oniki et al. 2009, Wilk et al., 2000, 2001), a conduction band offset as high as 1.5 eV (Lucovsky, 2002), and a wide band gap (~5.68 eV) (Robertson & Chen, 1999, Robertson, 2000).

In device fabrication processes, HfO$_2$ and ZrO$_2$ thin film layers are deposited by chemical vapor deposition (CVD) or physical vapor deposition (PVD) or sputtered onto Si substrates (Gao et al., 2000, Wang et al., 2005) using argon (Ar) and O$_2$ mixed gases. A sol-gel process offers various advantages for fabricating ZrO$_2$, HfO$_2$, ZrO$_2$–Y$_2$O$_3$ (YANG, 1996) and HfO$_2$ – Y$_2$O$_3$ (Nishide et al., 2000) thin films. The properties of a sol-gel-derived thin film depend on the composition of the sol solution, and residual H$_2$O may affect the performance of the film. Investigations of the basic structural and optical properties of sol-gel-derived HfO$_2$ films have shown that HfO$_2$ films formed on quartz substrates begin to crystallize at a firing temperature of 550 °C as determined from X-ray diffraction (XRD) patterns (Nishide et al., 2000). From the interplanar spacing they derived from the XRD patterns and a comparison of their data with data from a Joint Committee on Powder Diffraction Standards (JCPDS) card, they determined the crystalline phase of the sol-gel-derived HfO$_2$ film to be monoclinic. Recently, on the basis of high-resolution transmission electron microscopy (HRTEM) measurements in combination with results of electron beam nanodiffraction analyses, sol-gel-derived HfO$_2$ thin films on Si(001) wafers were found to crystallize in a monoclinic face-centered cubic (fcc) structure (Shimizu et al., 2004). Sol-gel-derived ZrO$_2$ thin films fired in air at 350 and 450 °C on Si(001) wafers are reported to be amorphous and around 9-10 nm in thickness. Crystallization occurs first at 550 °C as amorphous/tetragonal (011), and finally at 700°C, the ZrO$_2$ film crystallizes into tetragonal (011)/monoclinic ($\bar{1}$11) and (111) structures (Shimizu et al., 2009). Electrical characteristics have been evaluated using capacitors with an Al/ZrO$_2$ and/or HfO$_2$/Si sandwich structure. The leakage current and dielectric constant of the films have been examined using current-voltage (*I-V*) and capacitance-voltage (*C-V*) methods. On the basis of *C-V* characteristics, the dielectric constant (relative permittivity: ε_{ZrO2} and ε_{HfO2}) of sol-gel derived ZrO$_2$ and HfO$_2$ thin films fired in air were shown to be far higher than that of silicon dioxide (SiO$_2$: 3.9) (Shimizu et al., 2009, 2010). This chapter summarizes the characterizations of sol-gel-derived HfO$_2$, ZrO$_2$ and ZrO$_2$-Y$_2$O$_3$ thin films on Si(001) wafers with the aim of showing their suitability as alternative gate insulator materials in advanced CMOS devices.

2. Formation of sol-gel-derived HfO$_2$ on Si(001) wafers fired in air

A Hitachi HF-3000 transmission electron microscope (HRTEM) equipped with a cold type field-emission-gun (C-FEG) was used to obtain cross-sectional views of HfO$_2$ films on Si(001) wafers fired at 450 °C (amorphous state) and 700 °C (crystallized) [Figure 1 (a) and 1(b)]. The film fired at 700 °C did not show Moire patterns, indicating that the film consisted of single-crystal grains. Some subgrain boundaries or defects such as dislocations and twins were present, so overall the HfO$_2$ film fired at 700 °C was poly-crystalline.

Sol-gel-derived HfO$_2$ films on Si(001) wafers were evaluated by X-ray photoelectron spectroscopy (XPS). The XPS spectra of the Hf 4f [Figure 2(a)] and O 1s emissions [Figure 2(b)]
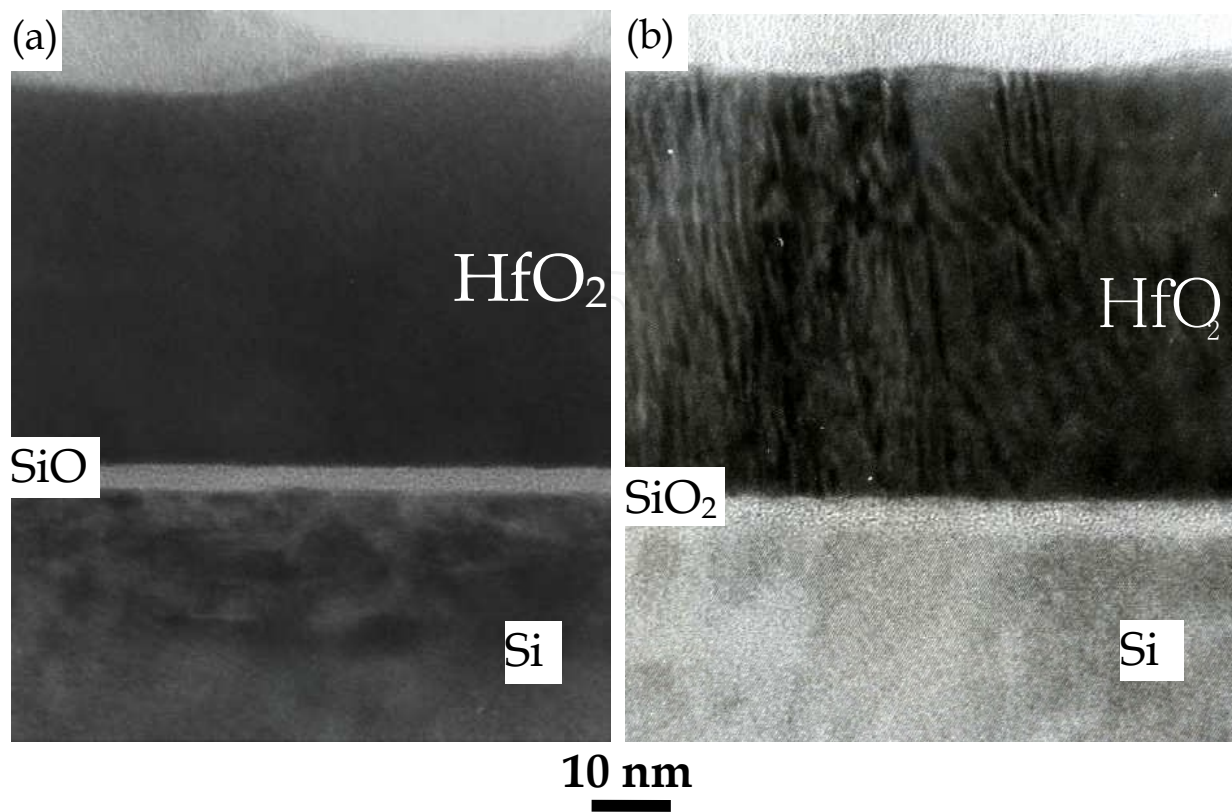
Characterization of Sol-Gel-Derived and Crystallized
HfO_2, ZrO_2, ZrO_2-Y_2O_3 Thin Films on Si(001) Wafers with High Dielectric Constant

317

Fig. 1. Cross-sectional views of HfO_2 films obtained by using a high-resolution TEM:
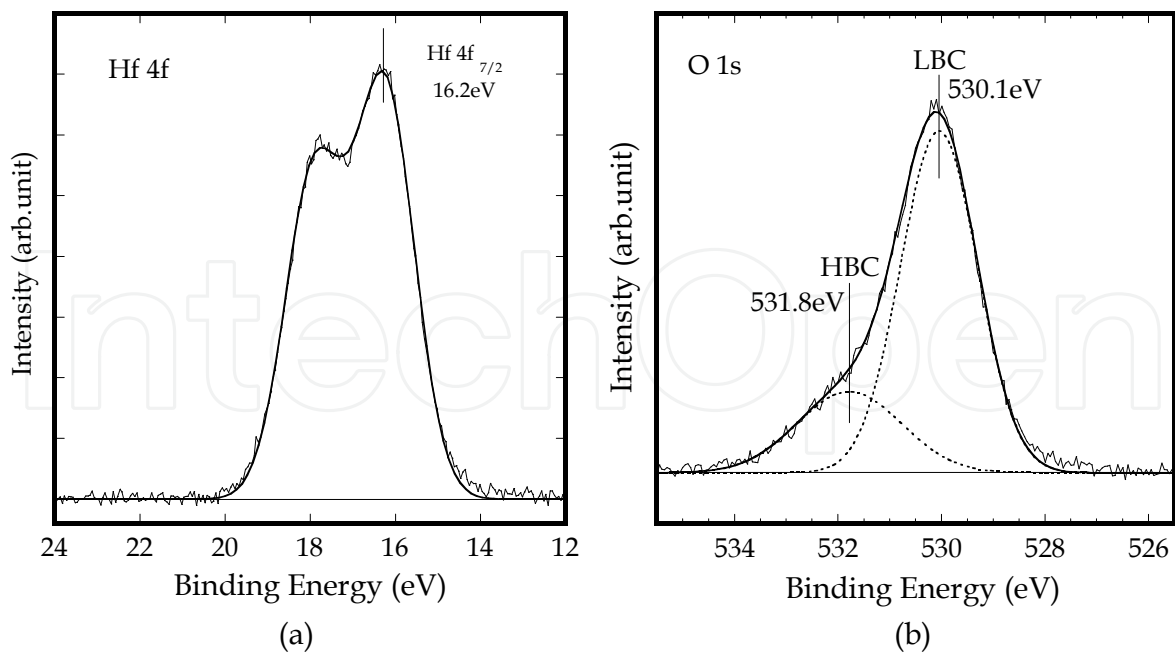(a) a HfO_2 film fired at 450 ℃ and (b) a HfO_2 film fired at 700 ℃ (Shimizu et al., 2004).

Fig. 2. XPS spectra of sol-gel-derived HfO_2 films. Solid lines are observed spectra and those
fitted by the nonlinear least-squares algorithm. Dashed lines for O 1s spectra have two
Gaussian peaks corresponding to Hf-OH (531.8 eV) and Hf-O (530.1 eV)
(Shimizu et al., 2007).

from the sol-gel-derived HfO$_2$ film fired at 450 °C indicated that the HfO$_2$ film was amorphous. The Hf 4f $_{7/2}$ line was determined to be at 16.2±0.1 eV, which is in good agreement with that of the bulk HfO$_2$ (Chiou et al., 2007, Moulder et al., 1995).

Crystallized HfO$_2$ films fired at temperatures of 550 and 700 °C showed similar XPS spectra regardless of whether they were amorphous or crystalline. The crystallization of sol-gel-derived HfO$_2$ films will be discussed later. The O 1s spectrum at 450 °C [Figure 2(b)] was separated into two Gaussian-Lorentzian features corresponding to two chemical states by using the nonlinear least-squares method. One large peak at 530.1 eV (designated as the low-binding-energy component: LBC) was from Hf-O bonds and the other low peak at 531.8 eV (designated as the high-binding-energy component: HBC) was from Hf-OH bonds near the bulk at the surface area. However, since the binding energy of H$_2$O was slightly larger (533.2 eV) than that of OH, the peak due to physisorbed H$_2$O may have been included in HBC in the present XPS measurements.

3. Formation of sol-gel-derived ZrO$_2$ on Si(001) wafers fired in air

The XPS spectra of the Zr 3d and O 1s emissions from sol-gel-derived ZrO$_2$ thin films fired at 350 °C are shown in [Figure 3(a)] and [Figure 3(b)], respectively. ZrO$_2$ thin films fired at 450, 550, and 700 °C were also evaluated and similar results were obtained. The Zr 3d $_{5/2}$ line was at 182.1±0.1 eV, which is in good agreement with that of the bulk ZrO$_2$ (182~182.5 eV) (Moulder et al., 1995). The O 1s spectrum at 350 °C was separated into two Gaussian-Lorentzian features corresponding to two chemical states by the nonlinear least-squares method [Figure 3(b)].
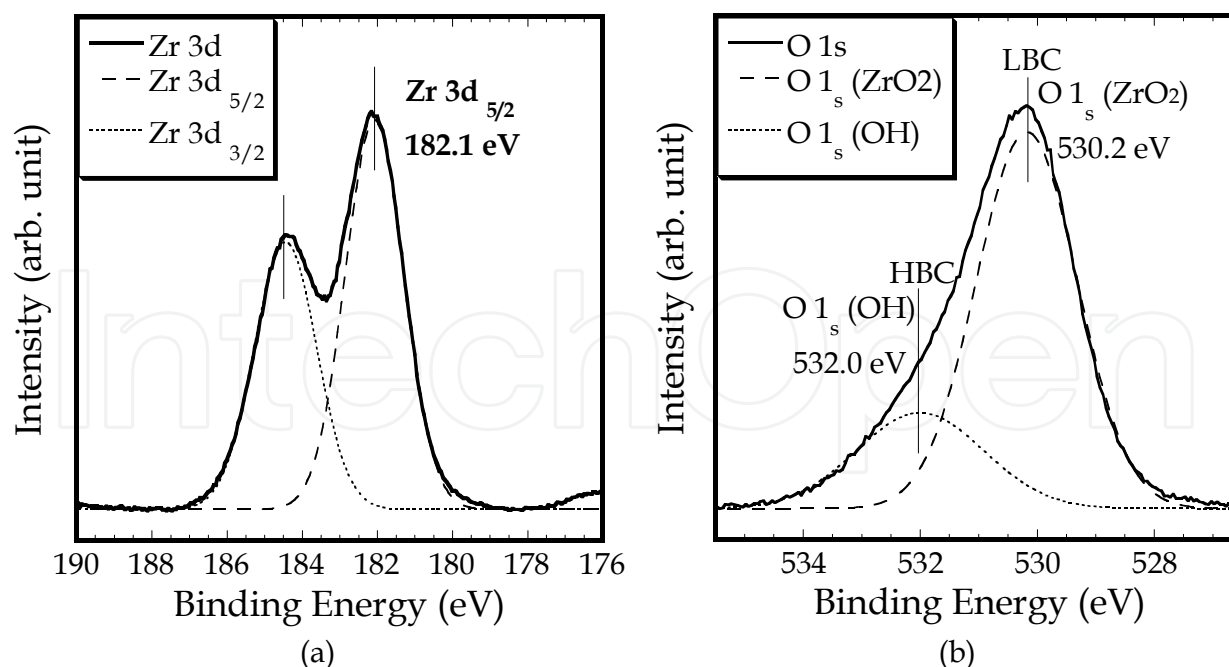

Fig. 3. XPS spectra of sol-gel-derived ZrO$_2$ thin films: (a) XPS Zr 3d spectrum and (b) XPS O 1s spectrum. Solid lines are the observed XPS spectra and dashed lines are for Zr 3d and O 1s spectra, which have two Gaussian peaks fitted by the nonlinear least-squares algorithm (Shimizu et al., 2009).

Characterization of Sol-Gel-Derived and Crystallized
HfO$_2$, ZrO$_2$, ZrO$_2$-Y$_2$O$_3$ Thin Films on Si(001) Wafers with High Dielectric Constant
319

One large peak at 530.2 eV (designated as the low-binding-energy component: LBC) was from Zr-O bonds and the other low peak at 532.0 eV (designated as the high-binding-energy component: HBC) was from Zr-OH bonds near the bulk at the surface area. However, since the binding energy of H$_2$O was slightly higher (533.2 eV) than that of OH, the peak due to physisorbed H$_2$O may [have been included in HBC?] in the present XPS measurements.

4. Crystallinity of sol-gel-derived HfO$_2$ thin films on Si(001) wafers

The XRD patterns for HfO$_2$ films on Si(001) wafers fired at 450, 550 and 700 ^{o}C were found to be in good agreement with previously reported results (Nishide et al., 2000) by using a spectrometer (Rigaku RAD-2 XRD) with CuKαradiation (Figure 4). Specifically, the film was still amorphous at 450 ^{o}C, and at 550 ^{o}C, new peaks appeared at 2θ = 28.4 and 31.8°, as well as small peaks in the region from 18 to 41°; these have been assigned to monoclinic crystalline HfO$_2$ components (Nishide et al., 2000). At 700 ^{o}C, the HfO$_2$ film was completely crystallized.
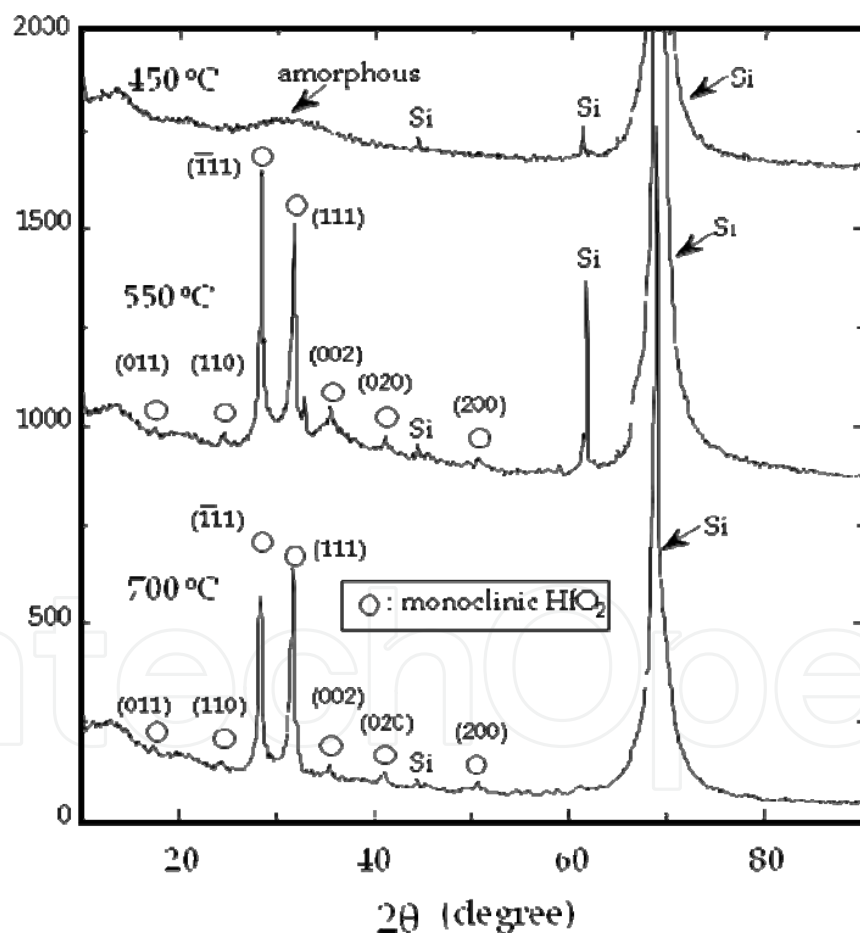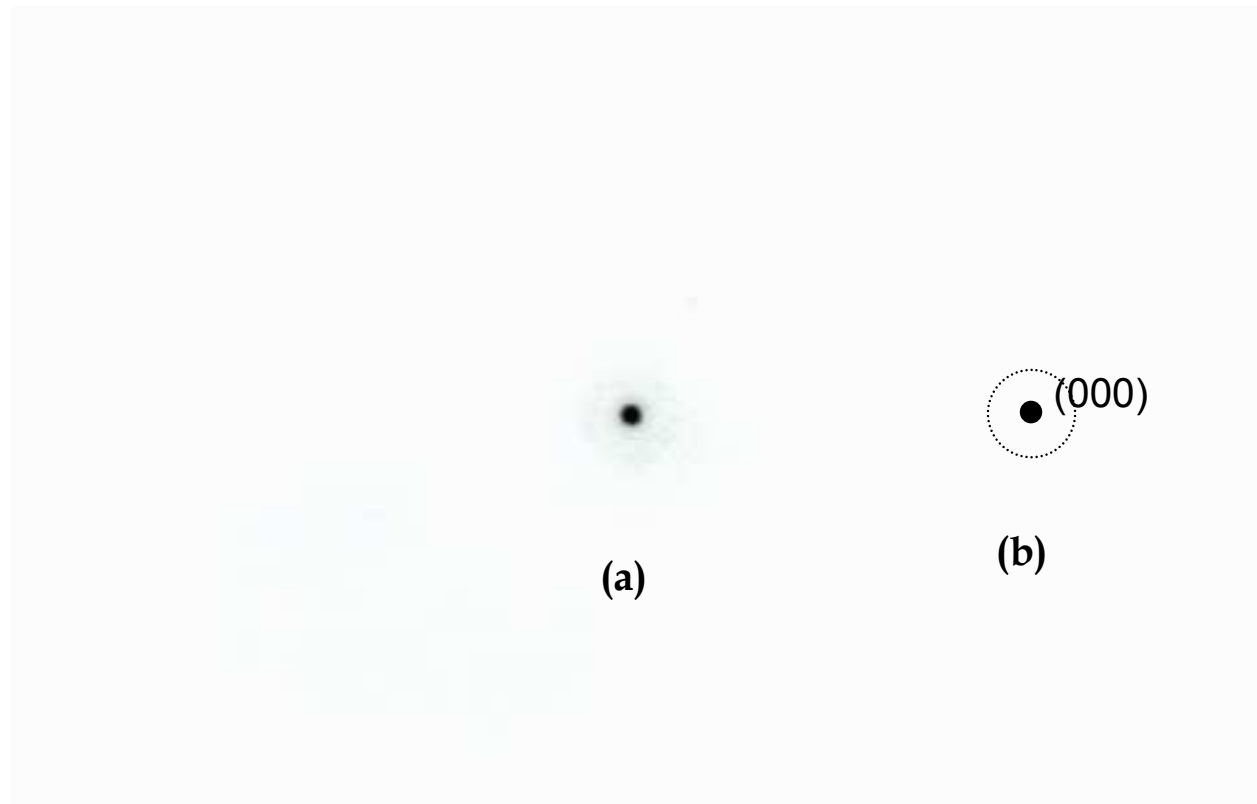

Fig. 4. XRD patterns obtained for HfO$_2$ films on Si(001) wafers fired at 450, 550 and 700 ^{o}C. Open circles indicate monoclinic HfO$_2$ (Shimizu et al., 2004).

In the electron beam (EB) nanodiffraction pattern for a cross section of the HfO$_2$ film fired at 550 ^{o}C, the Debye ring indicates the beginning of crystallization [Figure 5(a) and 5(b)].

Le=542 mm, λ=0.001969 nm at 300 KV, spot size=1.0 nm
(Debye ring: r_1=3.7 mm d_1=0.288 nm)

Fig. 5. Electron beam nanodiffraction pattern for the (110) plane of the HfO_2 film fired at 550 °C. r is the distance between diffracted spots in (111) in the HfO_2 film and d is the corresponding interplanar spacing (Shimizu et al., 2004).

The crystalline structure of the sample fired at 700 °C was determined by analyzing the EB nanodiffraction patterns as follows. First, the camera length (Le) of the HRTEM was determined on the basis of the EB nanodiffraction pattern for a cross section of the Si (110) substrate [Figure 6(a)] and the assignment of the diffraction spots [Figure 6(b)]. Using the data for Si from the International Centre for Diffraction Data, the camera length of the HRTEM was determined to be 542 mm (Shimizu et al., 2004).

Based on the EB nanodiffraction pattern for the sample fired at 700 °C [Figure 7(a)], the distances (r) between spots in the electron diffraction pattern appearing on the microscopic film were r_1 = 3.7 mm, r_2 = 3.4 mm and r_3 = 6.9 mm for the (111), (111) and (220) planes, respectively [Figure 7(b)]. The corresponding interplanar spacings were determined to be d_1 = 0.288 nm, d_2 = 0.314 nm and d_3 = 0.181 nm using the camera length. A detailed analysis of the alignment of the nanodiffraction spots, with the (000) spot at the center surrounded by 4 (111) spots and 2 (220) spots, together with the interplanar spacings, revealed that the HfO_2 film sintered at 700 °C had a monoclinic fcc (face centered cubic) structure. One of the measured interplanar spacings of the crystalline HfO_2 was 0.314 nm, which is in good agreement with the spacing of the Si (111) planes. This implies the possibility of the epitaxial growth of HfO_2 films on the Si (111) surface (Shimizu et al., 2004).

Characterization of Sol-Gel-Derived and Crystallized
HfO$_2$, ZrO$_2$, ZrO$_2$-Y$_2$O$_3$ Thin Films on Si(001) Wafers with High Dielectric Constant

321

Le=542 mm、 λ=0.001969 nm、 spot size=1.0 nm

r$_1$= 3.4 mm   d$_1$=0.314 nm (111)

r$_2$= 5.7 mm   d$_2$=0.191 nm (220)   Diamond
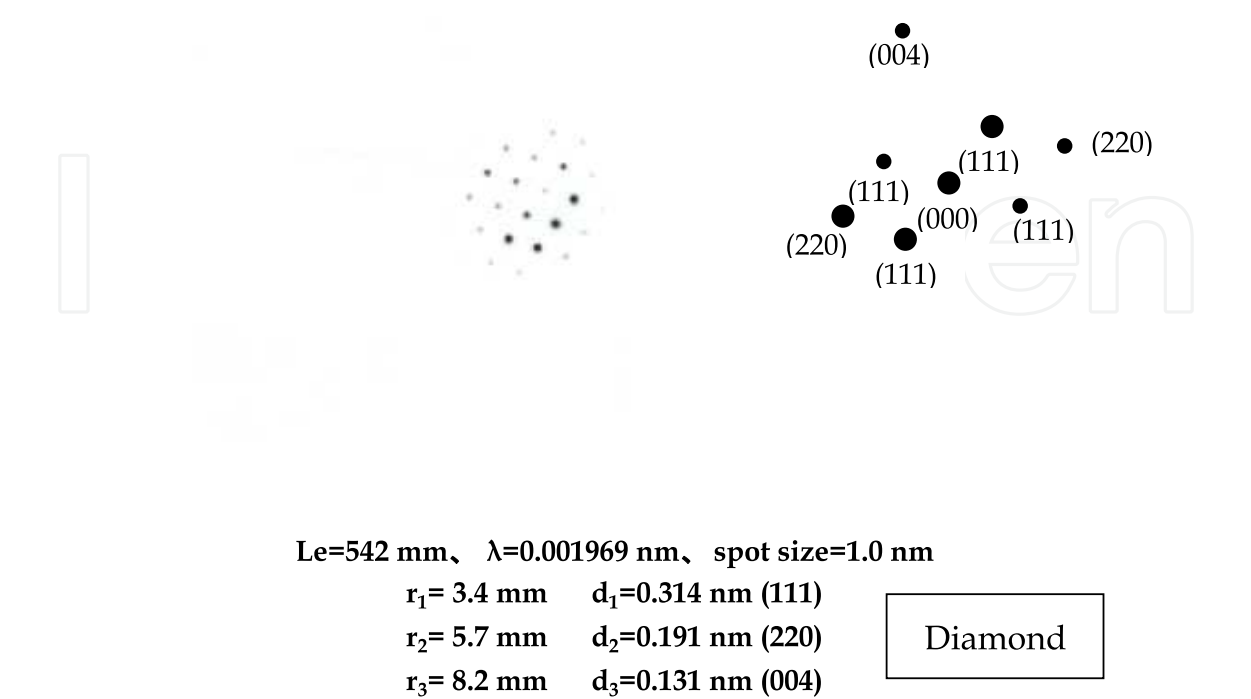
r$_3$= 8.2 mm   d$_3$=0.131 nm (004)

Fig. 6. Electron beam nanodiffraction patterns: (a) diffracted pattern on (110) plane of Si crystal and (b) schematic diffraction spots. *r* is the distance between diffracted spots in (111), (220) and (004) in the diamond structure and *d* is the corresponding interplanar spacing (Shimizu et al., 2004).
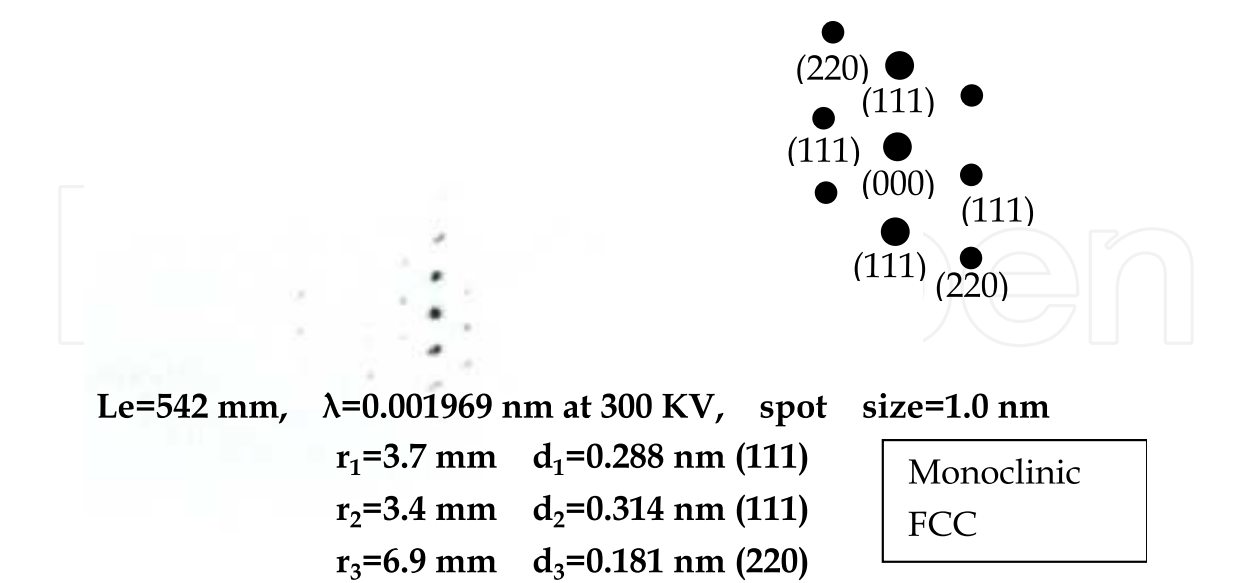
Le=542 mm, λ=0.001969 nm at 300 KV, spot size=1.0 nm

r$_1$=3.7 mm   d$_1$=0.288 nm (111)

r$_2$=3.4 mm   d$_2$=0.314 nm (111)   Monoclinic FCC

r$_3$=6.9 mm   d$_3$=0.181 nm (220)

Fig. 7. Electron beam nanodiffraction patterns: (a) diffracted pattern from a cross section of the HfO$_2$ film sintered at 700 °C and (b) schematic of the diffraction spots. *r* is the distance between diffracted spots in (111) and (220) in the HfO$_2$ film and *d* is the corresponding interplanar spacing (Shimizu et al., 2004).

5. Desorption of H_2O from sol-gel-derived HfO_2 and ZrO_2 thin films on Si(001) wafers during firing

During the firing of hafnia gel films, H_2O is not vaporized completely. Even after HfO_2 films are crystallized on the Si(001) surface, Hf-OH bonds and/or H_2O may be trapped between nanopores in HfO_2 films. Thus, the thermal properties, especially the desorption of H_2O from HfO_2 films, must be clarified after firing hafnia gel films. The electrical properties of sol-gel-derived HfO_2 films should also be characterized, in view of their possible application as gate insulators in next-generation CMOS devices.

Temperature-programmed desorption (TPD) is an excellent technique, not only for analyzing adsorbed gases on the surfaces of bulk sol-gel-derived HfO_2 films, but also for analyzing the species that evolve from the films.

5.1 Basic principles of TPD

TPD, also called thermal desorption spectroscopy, is essentially a method of analyzing desorped gases from samples heated under vacuum conditions using quadruple mass spectroscopy (QMS). The sample is heated by infrared light at a linear rate and evolved gases are introduced into a quadruple mass spectroscope that indicates the intensity of the signal according to the mass (m) and electric charge (z). TPD is now widely used to investigate the surfaces of ceramics and also semiconductors. In typical TPD spectra, the vertical axis shows the variation of the ion intensity of QMS (in amperes) for a specific m/z and the horizontal axis is the desorption temperature (Figure 8) (Nishide et al., 2004).
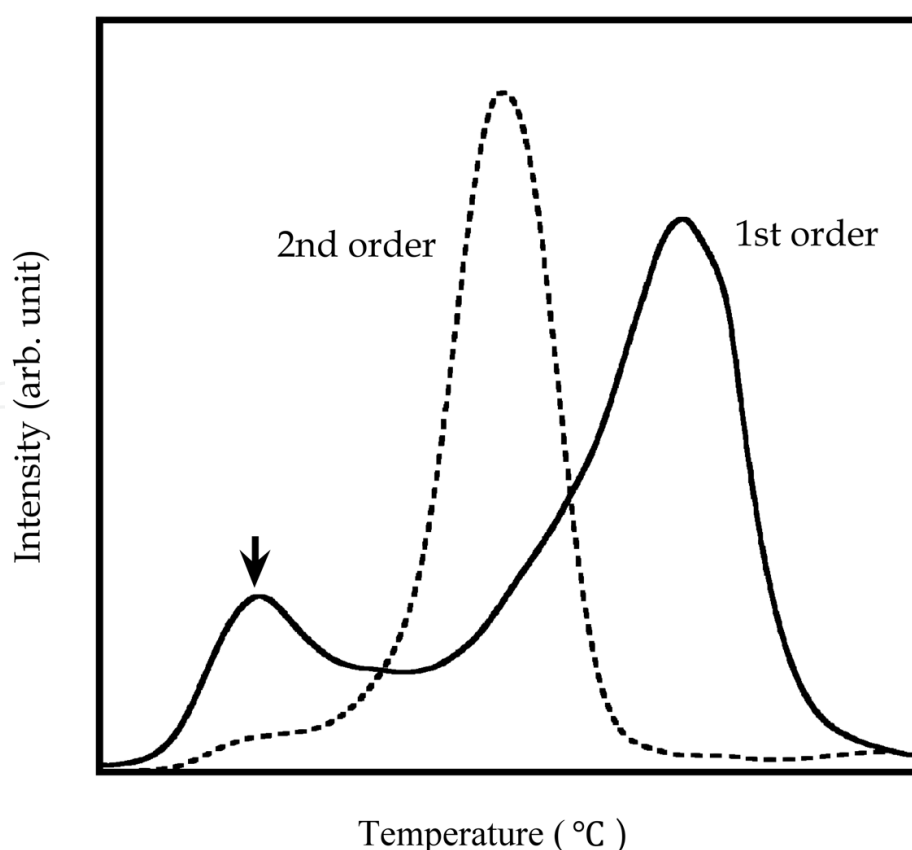

Fig. 8. Typical TPD curves plotted as a function of temperature (Shimizu et al., 2007).

Characterization of Sol-Gel-Derived and Crystallized
HfO$_2$, ZrO$_2$, ZrO$_2$-Y$_2$O$_3$ Thin Films on Si(001) Wafers with High Dielectric Constant

323

TPD curves can be obtained for various m/z's with increasing temperature, thereby enabling quantitative identification of species desorbed from materials and films. Simultaneously, the desorbed species can be physically and chemically analyzed. In addition, reaction rate analyses of desorbed gases can be performed. Figure 8 shows examples of (a) a nonsymmetrical TPD curve indicated by the solid line (the first-order reaction) and (b) a symmetrical TPD curve indicated by the dashed line (the second-order reaction) as a function of temperature. The arrow on the nonsymmetrical TPD curve corresponds to the evolution of physisorbed and chemisorbed H$_2$O, which is specified to be a liquid such as water and water molecules hydrogen-bonded to Si-OH bonds at nanopore sites in the films (Hirashita et al., 1993).

For chemical-vapor-deposited SiO$_2$ films, three distinct H$_2$O desorption states have been defined (Hirashita et al., 1993). They are physisorbed H$_2$O evolved at temperatures between 100 and 200 °C and chemisorbed H$_2$O evolved at temperatures between 150 and 300 °C in a TPD measurement. The higher desorption peak between 350 and 650 °C is ascribed to Si-OH bonds formed during film growth. Thus, TPD is a useful technique for evaluating surfaces and thin films of ceramics and semiconductors.

5.2 TPD spectral analyses of sol-gel-derived HfO$_2$ thin films

The desorption of H$_2$O (m/z = 18) that evolved from sol-gel-derived HfO$_2$ films on Si was analyzed by TPD (Figure 9). The HfO$_2$ films were fired at 450, 550, and 700 °C for 30 min. The vertical axis indicates the current value of QMS. The small peaks below 200 ℃ are due to the physisorbed H$_2$O (mere adsorption of H$_2$O) on the surface of the HfO$_2$ films and/or chemisorbed Hf-OH in the bulk at the surface area. Based on experiments, the small peaks are attributed to the adsorption of

H$_2$O immediately after the samples were taken out of the furnace and the amount of desorbed water (i.e., adsorbed water) saturated. The desorption states of physisorbed H$_2$O and/or chemisorbed Hf-OH bonds originate from liquid-like water, water molecules, and Hf-OH bonds at nanopore sites in the HfO$_2$ films.

Regarding the major peaks in the TPD spectra, two types of desorption curves are observed at temperatures higher than 200 °C. One has the form of a symmetrically shaped peak (Lorentzian distribution shoulder as shown by the dashed line) at around 320 °C (fired at 450 °C), which is reaction-controlled (Soraru, 2002) (the second-order reaction) (Nishide et al. 2004). The other consists of nonsymmetrical peaks at approximately 420 °C (fired at 550 °C) and 480 °C (fired at 700 °C) which are diffusion-controlled (the first order reaction) (Nishide et al., 2004). When the curve is symmetrical in shape, the peak at around 320 °C (fired at 450 °C) is not caused by physisorbed H$_2$O from the nanopores at the surface area, but can be ascribed to the associated desorption of chemisorbed water (Hf-OH) from the gel film, resulting in the formation of H$_2$O during firing, which is specified to be the second-order reaction (Nishide et al., 2004).

For the samples fired at 450 °C, Hf-OH bonds in the HfO$_2$ film bulk convert to HfO$_2$ and/or H$_2$O during heating and the resulting H$_2$O contributes to the major desorption peak in the TPD curve [Figure 10(a) and 10(b)], as a result of the following reaction
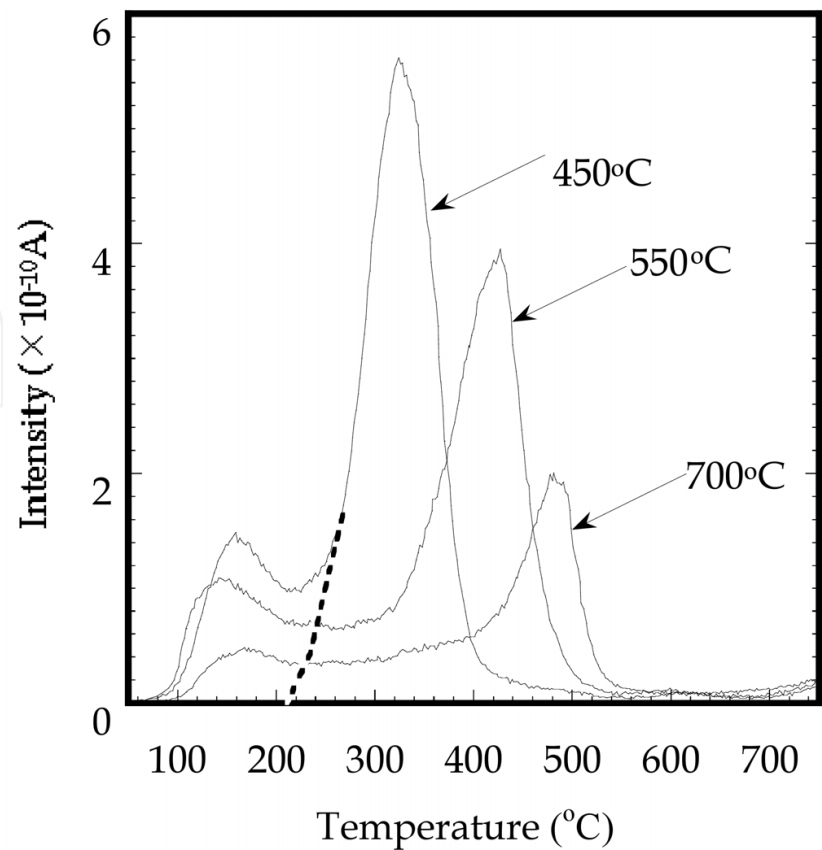
$$\equiv \text{Hf-OH HO-Hf} \equiv \ \rightarrow \ \equiv \text{Hf-O-Hf} \equiv \ + \text{H}_2\text{O}. \tag{1}$$
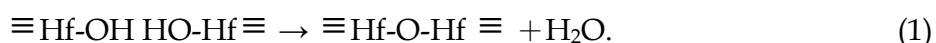
Fig. 9. TPD curves of H_2O (m/z = 18) that evolved from sol-gel-derived HfO_2 films on Si when fired at 450, 550, and 700 °C for 30 min (Shimizu et al., 2007).
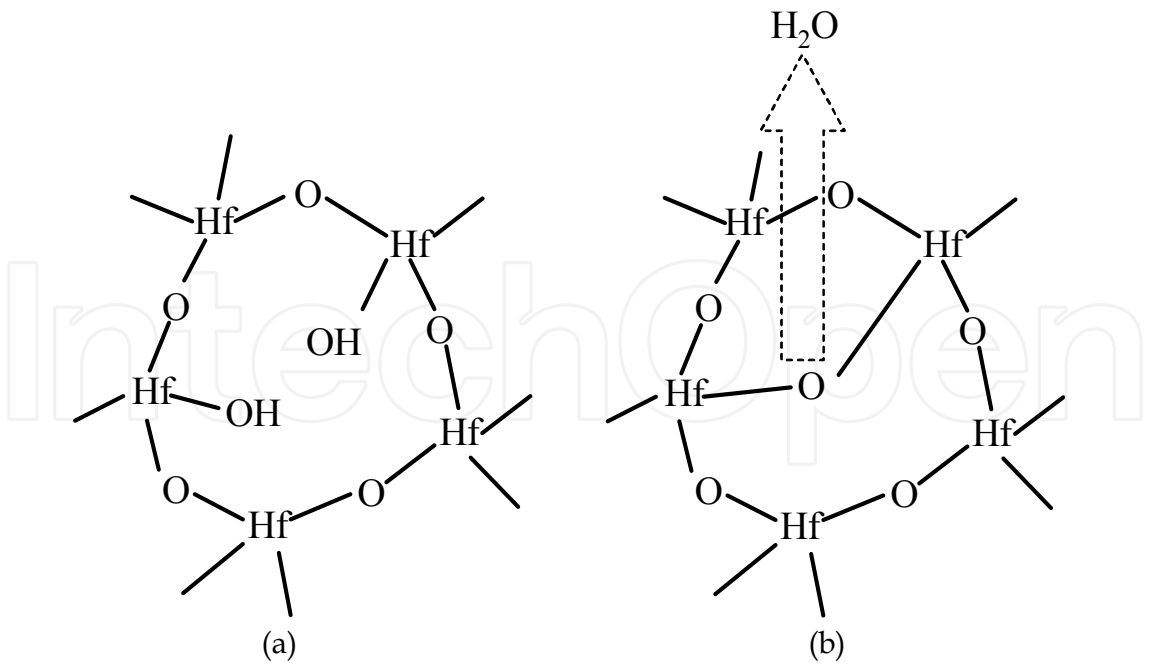

Fig. 10. A schematic speculation of H_2O desorption from HfO_2 films during TPD measurements for both amorphous and crystalline states. (a) Hf-OH bonds in the sol-gel derived HfO_2 films and (b) the formation of desorbed H_2O as a result of the following reaction: $\equiv$ Hf-OH HO-Hf $\equiv$ $\rightarrow$ $\equiv$ Hf-O-Hf $\equiv$ + H_2O (Shimizu et al., 2007).

Characterization of Sol-Gel-Derived and Crystallized
HfO$_2$, ZrO$_2$, ZrO$_2$-Y$_2$O$_3$ Thin Films on Si(001) Wafers with High Dielectric Constant

325

In contrast, most of the HfO$_2$ films fired at 700 °C crystallized, where Hf-OH bonds in the films are conjectured to be tightly locked between crystallized grains and incorporated H$_2$O needs greater energy to percolate by the diffusion control mechanism through small gaps between grains. Therefore, in the TPD curve, the H$_2$O desorption peak shifts to higher temperatures and decreases steadily as the firing temperature increases.

5.3 Adsorption mechanism of physisorbed H$_2$O clarified by TPD using sol-gel-derived ZrO$_2$ thin films

To clarify whether the small peaks (small protrusions) between 100 and 200 °C in the TPD curves were due to physisorbed H$_2$O (mere adsorption of H$_2$O) on the surface of the ZrO$_2$ thin films and/or chemisorbed Zr-OH in the bulk at the surface area (Figure 11), the following three experiments were carried out (Shimizu et al., 2009). First (process ①), a sample immediately after firing at 350 °C for 30 min was measured by TPD until 350 °C and then (process ②) successively measured by TPD again from room temperature to 350 °C; finally (process ③), the sample was exposed to air for 59 h and then measured by TPD from room temperature to 700 °C. The TPD curve of H$_2$O in process ① was in good agreement with the typical curve of a ZrO$_2$ thin film fired at 350 °C for 30 min. No peaks were observed in process ②, indicating that the small protrusions and major peak vanished during heating
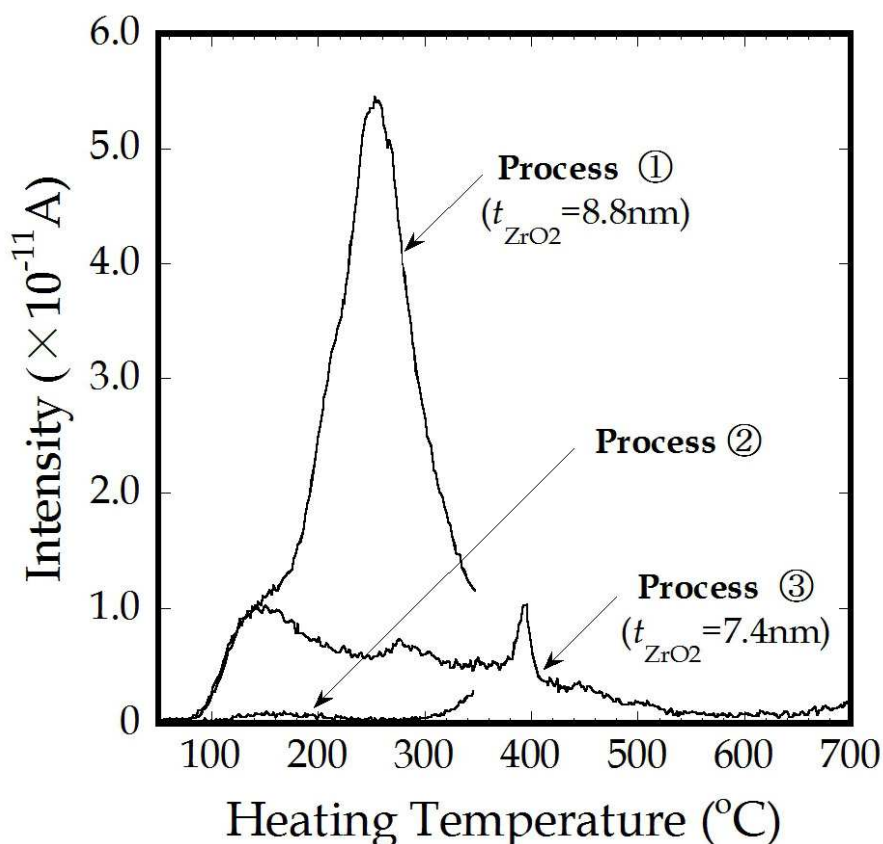

Fig. 11. TPD curves for processes (1), (2), and (3). In process (1), a sample immediately after firing at 350 °C for 30 min was measured by TPD until 350 °C, followed by process (2) in which the sample was successively measured by TPD again from room temperature to 350 °C; finally, process (3) in which the sample was exposed to air for 59 h and then measured by TPD from room temperature to 700 °C (Shimizu et al., 2009).

until 350 °C in the first TPD measurement. In contrast, in process ③, the small protrusions between 100 and 200 °C appeared again. This result provides evidence that the small peaks (small protrusions) were caused by adsorption of H_2O immediately after the samples were taken out of the furnace and that the amount of desorbed water (i.e., adsorbed water) saturated during the exposure time. Thus, the small protrusions in the TPD curves can be attributed to physisorbed H_2O and/or chemisorbed Zr-OH bonds at the surface area.

6. Characterization of sol-gel-derived HfO₂ thin films on Si(001) wafers dependent on sol solution: "HCOOH sol" and "HNO₃ sol" HfO₂ thin films

6.1 Crystallization temperature dependent on sol solution of HfO₂ thin films on Si(001) wafers

In sol-gel-derived HfO_2 thin films on Si(001) wafers, the crystallization temperature depends on the composition of the sol solution. Upon preparing the sol solution, (a) a formic acid (HCOOH) or (b) a nitric acid (HNO_3) is used as the catalyst for $Hf(OH)_4$ to form a soluble sol in H_2O, resulting in a hafnia sol solution.
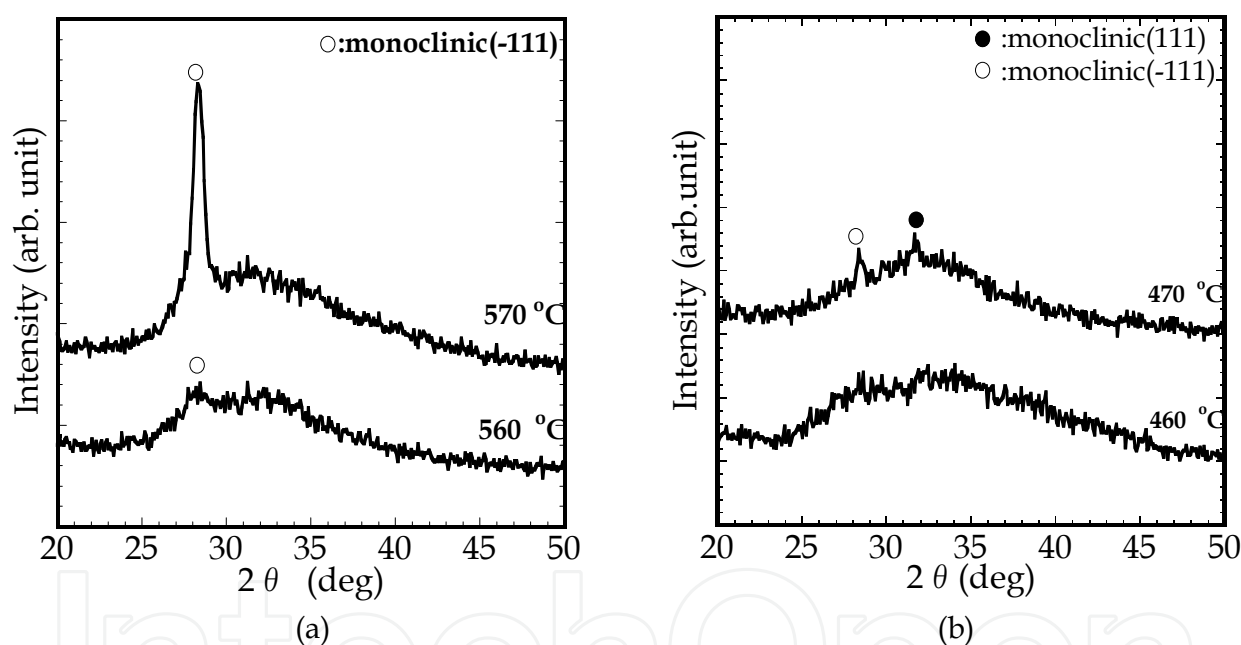

Fig. 12. (a) XRD patterns of "HCOOH sol" HfO_2 films on Si fired at 560 and 570 ᵒC and (b) XRD patterns of "HNO₃ sol" HfO_2 films on Si fired at 460 and 470 ᵒC (Shimizu et al., 2010).

In the X-ray pattern for "HCOOH sol" HfO_2 films fired at temperatures below 560 °C, only halo patterns representing the amorphous state were observed. At 560 °C [Fig. 12(a)], a small diffraction peak was observed at $2\theta = 28°$ in the halo pattern. At 570 °C, the diffraction peak at $2\theta = 28°$ became clearer and higher, indicating that partial crystallization from the amorphous state commenced at 560 °C. The observed diffraction peak was identified to correspond to monoclinic (111) (JCPDS card) and full crystallization was attained at 700 °C.

In contrast, "HNO₃ sol" HfO_2 films fired at 460 °C showed no diffraction peaks (only halo patterns were observed). At 470 °C, two diffraction peaks were identified, corresponding to the monoclinic structures ($\bar{1}11$) and (111) according to the JCPDS card [Fig. 12(b)]. By using

Characterization of Sol-Gel-Derived and Crystallized
HfO$_2$, ZrO$_2$, ZrO$_2$-Y$_2$O$_3$ Thin Films on Si(001) Wafers with High Dielectric Constant

327

a HNO$_3$ solution as the catalyst, the crystallization temperature was reduced to less than 470 °C compared with 560 °C for the "HCOOH sol" HfO$_2$ films. The lattice interplanar distances calculated using the Bragg equation were 0.319 and 0.286 nm, in contrast to the reported values of 0.314 and 0.288 nm, respectively (Shimizu et al., 2004). These results probably differed from the crystallization temperature for the monoclinic structure (111) (Nishide et al., 2000) because different sol solutions were employed in each case. The "HCOOH sol" HfO$_2$ films remained in the amorphous state up to a higher temperature (560 °C) than the "HNO$_3$ sol" films (crystallized at 470 °C). Based on TPD measurements, HCOOH and HNO$_3$ desorb at temperatures below 350 °C, indicating that an intrinsic amorphous HfO$_2$ film without using a catalyst for either film stably exists above 350 °C (Shimizu et al., 2010).

6.2 Thicknesses and refractive indexes dependent on sol solution of HfO$_2$ thin films

The thickness of the sol-gel-derived HfO$_2$ films decreased with increasing firing temperature (Figure 13). It is seen that the smallest thickness was 6 nm for the "HCOOH sol" HfO$_2$ film fired at 700 °C, which is about 1 nm thinner than the thinnest "HNO$_3$ sol" HfO$_2$ film. The difference is due to the properties of the catalyst used and this result shows that the "HCOOH sol" HfO$_2$ film may be suitable for use as the gate insulator of highly integrated CMOS devices. However, its electrical performance should be superior to that of conventional HfO$_2$ films.
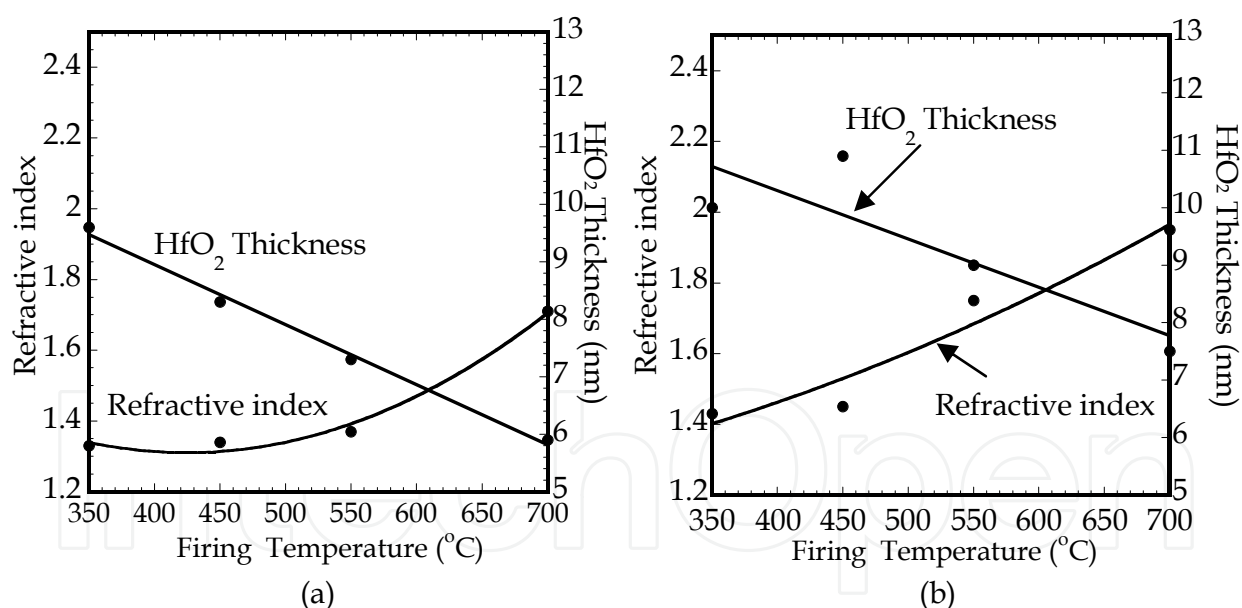

Fig. 13. Thicknesses and refractive indexes of sol-gel-derived HfO$_2$ films based on both (a) "HCOOH sol" and (b) "HNO$_3$ sol" fired at 350, 450, 550, and 700 °C for 30 min in air (Shimizu et al., 2010).

The refractive indexes began to increase at approximately 550 °C for the "HCOOH sol" film and at 450 °C for the "HNO$_3$ sol" film. These temperatures are in good agreement with those at which crystallization occurs, as obtained by XRD analysis [Figures 12(a) and 12(b)]. The maximum refractive indexes obtained were 1.70 for the "HCOOH sol" film and 1.95 for the "HNO$_3$ sol" film, although the reported value for the HfO$_2$ crystal (monoclinic) is 2.19. The

packing densities of the HfO_2 films were calculated using the Lorentz-Lorentz equation (Nishide et al., 2001),

$$p = \frac{n_f^2 - 1}{n_f^2 + 2} \times \frac{n_m^2 + 2}{n_m^2 - 1} , \qquad (2)$$

where p is the packing density, n_f is the refractive index of the film, and n_m is the refractive index of the crystal. The calculated packing densities indicated that nanopores remained in the amorphous state. However, upon the crystallization of the film, the packing densities became greater than those in the amorphous state in both the "HCOOH sol" and "HNO_3 sol" HfO_2 films.

6.3 Surface morphologies of HfO_2 layers for both "HCOOH sol" and "HNO_3 sol" HfO_2 films

Images of surface microstructures were obtained with an atomic force microscope (AFM) for both "HCOOH sol" and "HNO_3 sol" HfO_2 films fired at 350, 450, 550, and 700 °C (Figures 14 and 15). The progress of the microstructure development depended on the firing temperature. The surface of the "HCOOH sol" HfO_2 thin films fired at 350, 450, and 550 °C showed homogeneous glass-like structures. The root mean square (RMS) surface roughness was determined to be 0.13, 0.14, and 0.15 nm at firing temperatures of 350, 450 and 550 °C, whereas it was 0.34 nm at 700 °C, which indicated the presence of grain boundaries caused by crystallization. These values are in good agreement with the XRD and refractive index results. For the "HNO_3 sol" HfO_2 films, the RMS values were 0.14 and 0.15 nm at firing temperatures of 350 and 450 °C, respectively. At firing temperatures of 550 and 700 °C, the RMS values were 0.17 and 0.34 nm, resulting in grain boundaries due to crystallization. In this case, the surface roughness was also due to crystallization.

6.4 TPD spectral analyses of sol-gel-derived HfO_2 thin films based on "HCOOH sol" and "HNO_3 sol"

The desorption of H_2O ($m/z = 18$) was analyzed by TPD for both "HCOOH sol" and "HNO_3 sol" HfO_2 films on Si(001) wafers fired at 350, 450, 550, and 700 °C for 30 min [Figures 16(a) and 16(b)]. The vertical axis indicates the QMS current and the horizontal axis shows the heating temperature of the samples in the TPD chamber. The film thicknesses ranged approximately between 6 to 10 nm. The overall intensities of the desorption of H_2O in the TPD curves are related to both the "HCOOH sol" and "HNO_3 sol" HfO_2 films. The intensity of both TPD curves decreased with increasing firing temperature. The "HCOOH sol" HfO_2 films fired at 350, 450, and 550 °C, which were amorphous, showed small peaks at approximately 500 °C in the TPD curves. These peaks are presumably associated with crystallization during heating in the TPD chamber, because no corresponding peak was observed in the film fired at 700 °C (crystallization temperature: 560 °C).

TPD curves for the HfO_2 thin films fired at 350 °C using the "HCOOH sol" and "HNO_3 sol" on Si are separated into five Gaussian waveforms shown by dashed lines [Figure 17(a) and 17(b)]. Component (a) is thought to be due to H_2O physically adsorbed (simple adsorption of H_2O) on the surface of the HfO_2. Component (e) can be ascribed to the desorption of H_2O through nanopores in the crystallized HfO_2 film. Component (b) is probably due to the
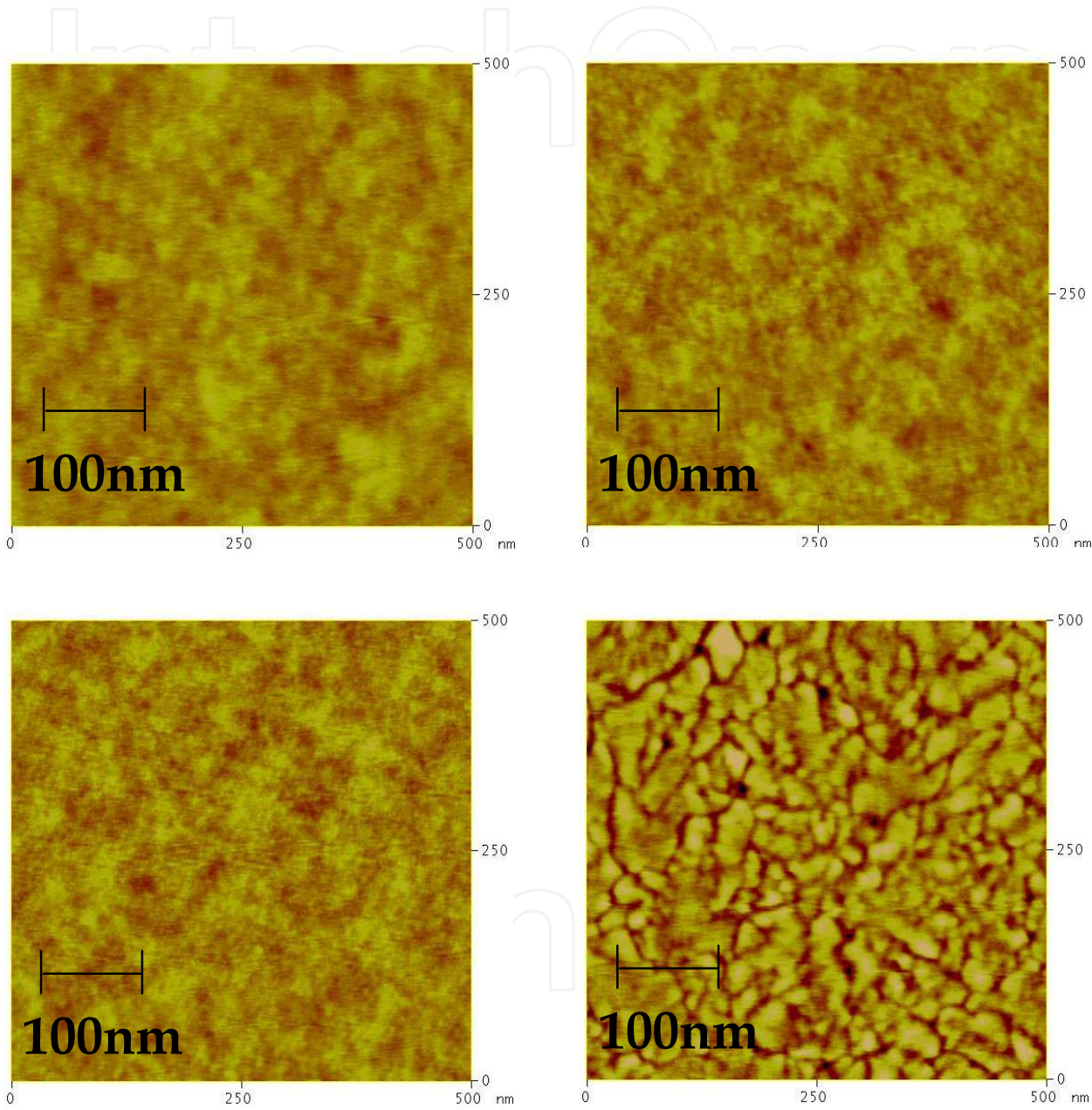
Characterization of Sol-Gel-Derived and Crystallized
HfO$_2$, ZrO$_2$, ZrO$_2$-Y$_2$O$_3$ Thin Films on Si(001) Wafers with High Dielectric Constant

329

Fig. 14. AFM images showing the surface microstructures of "HCOOH sol" HfO$_2$ thin films fired at (a) 350, (b) 450, (c) 550 and (d) 700 ᵒC (Shimizu et al., 2010).
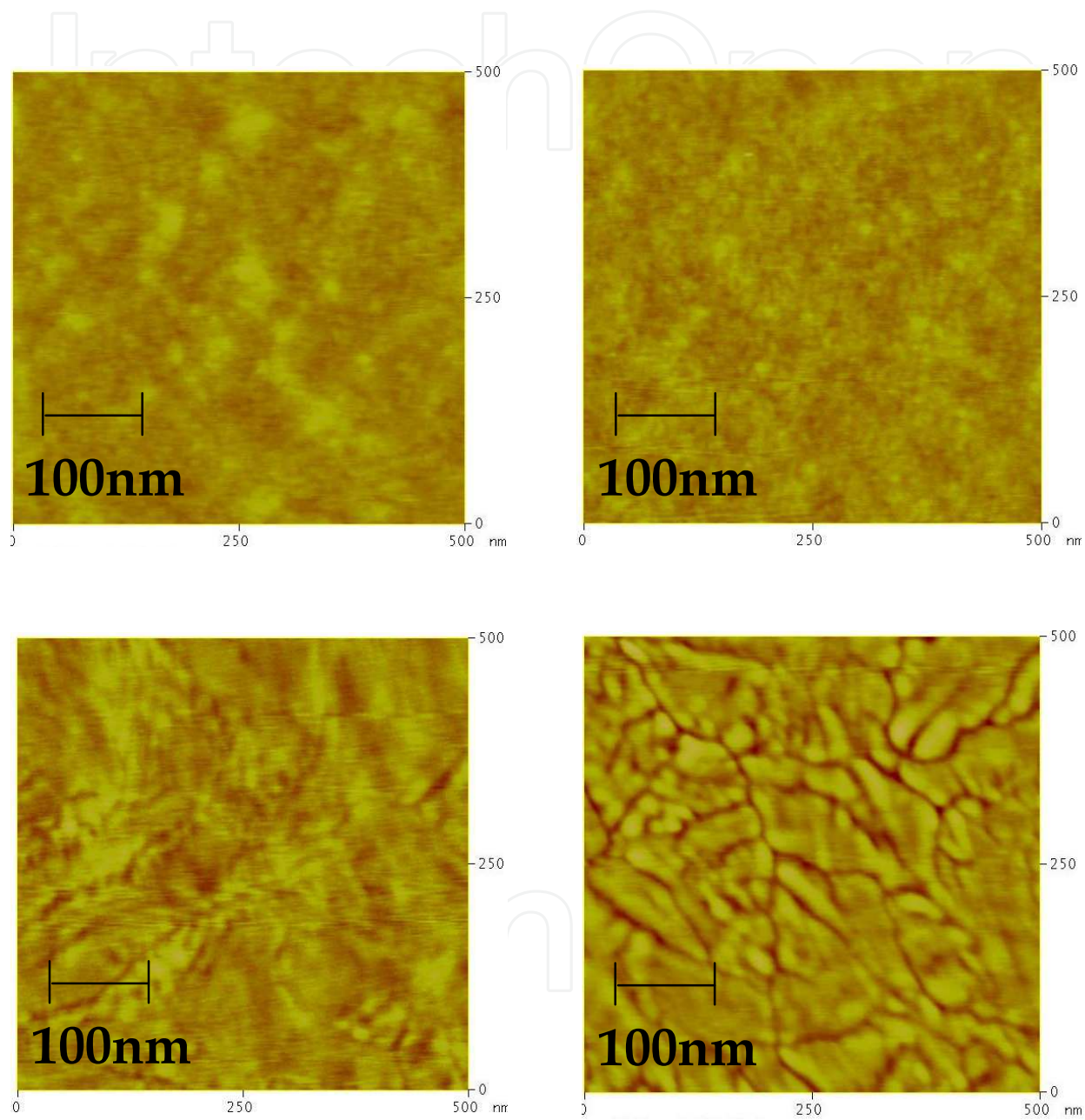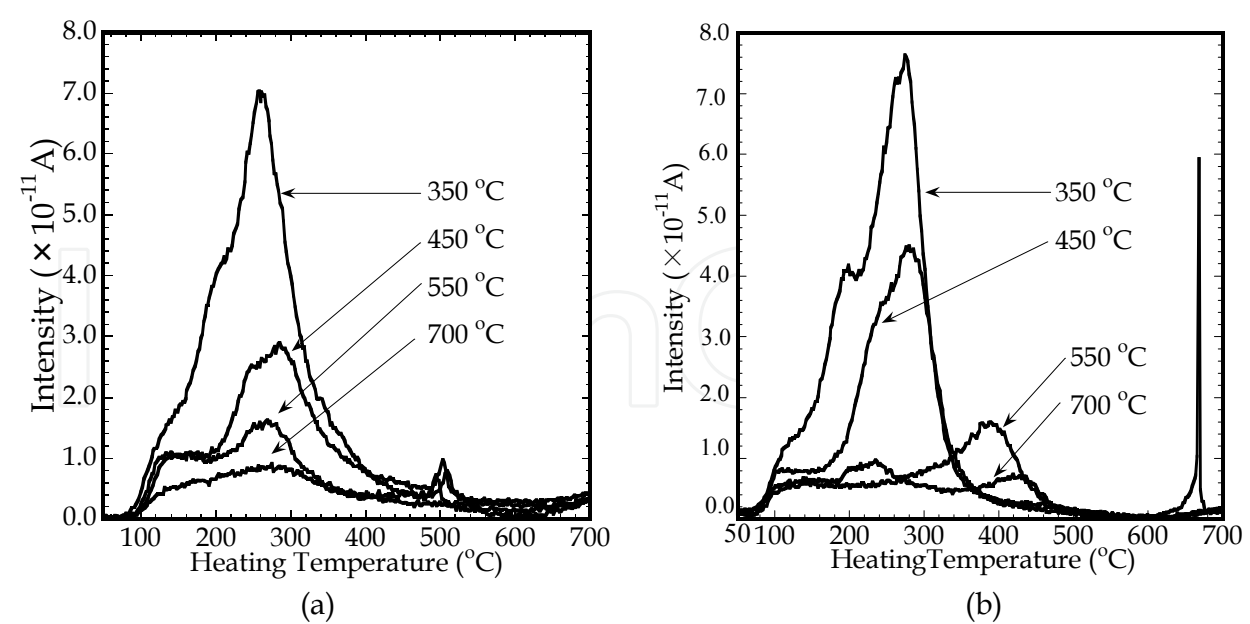
Fig. 15. AFM images showing the surface microstructures of "HNO$_3$ sol" HfO$_2$ thin films fired at (a) 350, (b) 450, (c) 550 and (d) 700 ^{o}C (Shimizu et al., 2010).

Fig. 16. TPD curves of H_2O (m/z = 18) released from sol-gel-derived HfO_2 thin films fired at 350, 450, 550, and 700 °C for 30 min: (a) HfO_2 films using "HCOOH sol" and (b) HfO_2 films using "HNO₃ sol" on Si. The vertical axis indicates the QMS current and the horizontal axis shows the heating temperature of the samples in the TPD chamber (Shimizu et al., 2010).
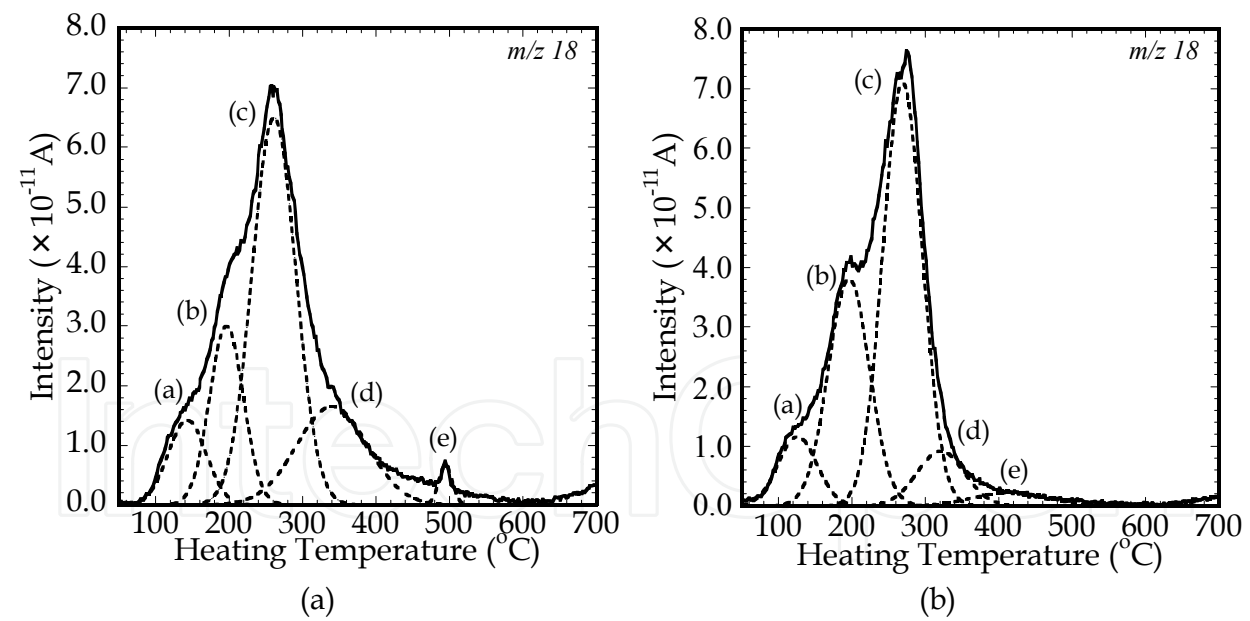

Fig. 17. TPD curves for sol-gel-derived HfO_2 thin films fired at 350 °C using
(a) "HCOOH sol" and (b) "HNO₃ sol" on Si, separated into five Gaussian waveforms shown by the dashed lines (Shimizu et al., 2010).

desorption of H_2O and/or chemically adsorbed Hf-OH bonds on the surface. On the other hand, the desorption of O in the TPD curves has main peaks at ~260 °C and subpeaks at ~350 °C, corresponding to the peak temperatures of components (c) and (d). For components (c) and (d), the desorption of the chemically adsorbed Hf-OH bonds and/or a small amount

of O can occur from the nanopores of the HfO$_2$ film via the reaction OH + OH→H$_2$O + O. In addition, the H$_2$O desorption of chemically adsorbed Hf-OH may occur by the abovementioned reaction ($\equiv$ Hf-OH $+$ HO-Hf $\equiv$ $\rightarrow$ $\equiv$ Hf-O-Hf $\equiv$ $+$H$_2$O).

HCOOH and/or HNO$_3$ adsorbs or bonds on the surface of the sol. In the "HCOOH sol", HCOOH ions form a bridge structure coordinated with Hf ions (Nishide et al., 2004). In the TPD measurements performed after the firing process, HCOOH and HNO$_3$ were found to desorb at less than 350 ^{o}C. Thus, "HCOOH sol" and "HNO$_3$ sol" HfO$_2$ films in the amorphous state without an acid exist stably on Si wafers above 350 ^{o}C. This result may affect the *I-V* characteristics, as will be discussed later.

On the basis of the foregoing results, a speculative schematic diagram of physically adsorbed H$_2$O and the chemically adsorbed Hf-OH attached to a sol-gel-derived HfO$_2$ film is shown in Fig. 18. The gaps in the figure correspond to nanopores.
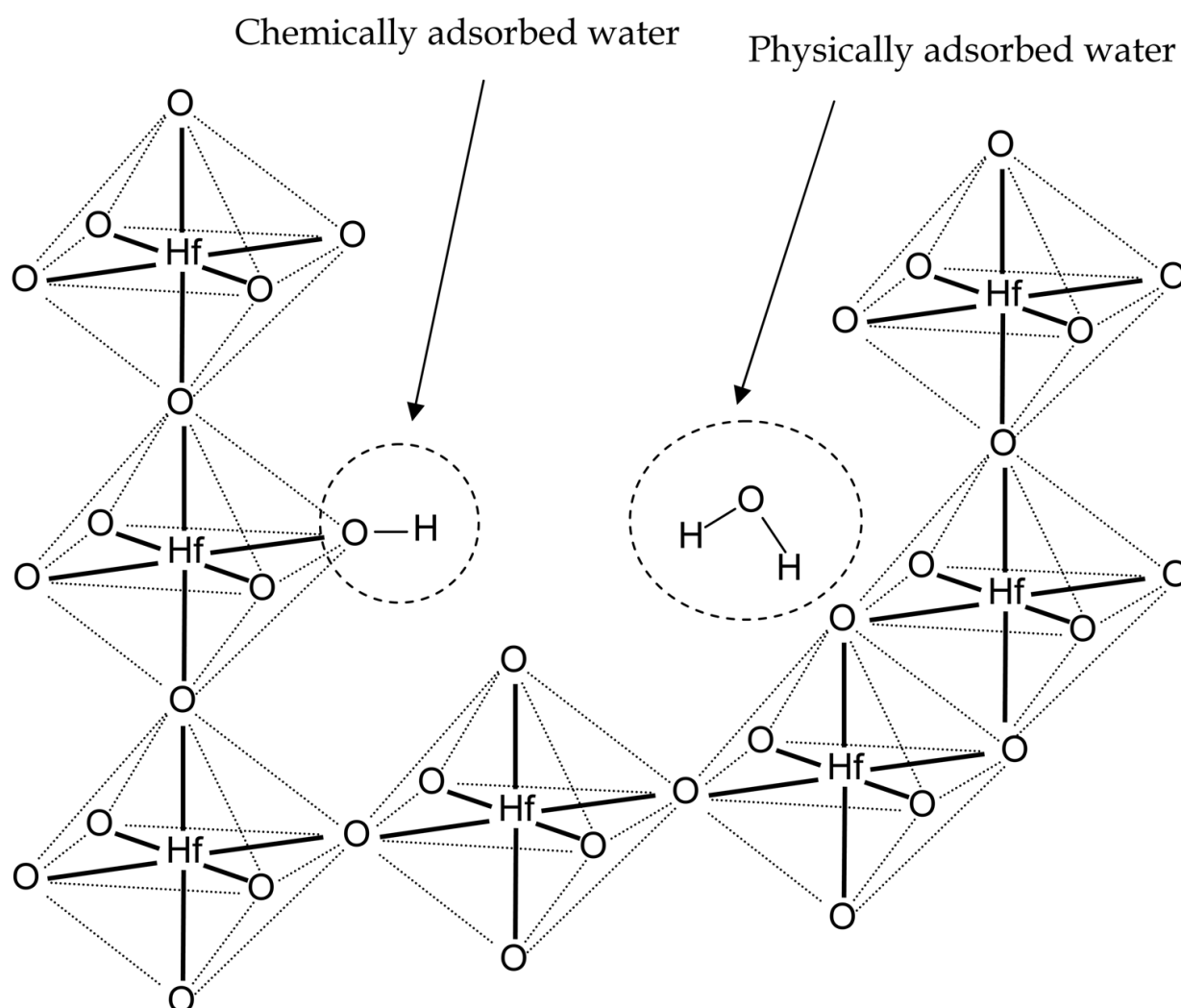

Fig. 18. Speculative schematic diagram of physically adsorbed H$_2$O and chemically adsorbed Hf-OH attached within the sol-gel-derived HfO$_2$ film (Shimizu et al., 2010).

Characterization of Sol-Gel-Derived and Crystallized
HfO$_2$, ZrO$_2$, ZrO$_2$-Y$_2$O$_3$ Thin Films on Si(001) Wafers with High Dielectric Constant
333

6.5 Electrical characterization of both "HCOOH sol" and "HNO$_3$ sol" HfO$_2$ thin films on Si(001) wafers

To measure the electrical characteristics (i.e., *I-V* and *C-V* characteristics) of both "HCOOH sol" and "HNO$_3$ sol" HfO$_2$ thin films on Si(001) wafers, a 0.4-mm-diameter aluminum (Al) electrode was deposited on the surface of the films. Al/HfO$_2$/SiO$_2$/n-Si capacitors were fabricated on the Si wafers using a shadow mask in a vacuum. Using these capacitors, the *I-V* characteristics, i.e., the current vs electric field relationships, were investigated for the "HCOOH sol" and "HNO$_3$ sol" HfO$_2$ thin films fired at 350, 450, 550, and 700 °C in air.

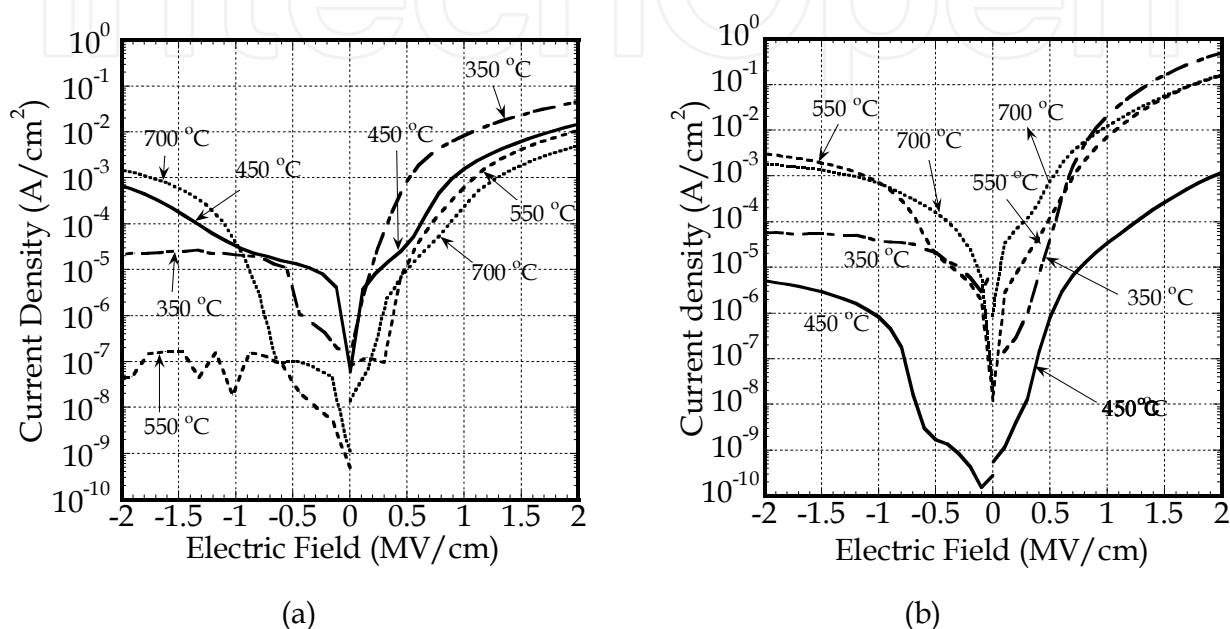
(a)	(b)

Fig. 19. *I-V* characteristics of HfO$_2$ thin films fired at 350, 450, 550, and 700 °C in air using both (a) "HCOOH sol" and (b) "HNO$_3$ sol (Shimizu et al., 2010)".

The absolute values of the reverse bias are plotted in Figure 19. For the "HCOOH sol" HfO$_2$ thin films, a small bias dependence on firing temperature was detected for the forward bias condition. In contrast, for the reverse bias condition, the smallest leakage current was observed at a firing temperature of 550 °C (amorphous film) for which the leakage current was ~10^{-7} A/cm^2 in an electric field of -2 MV/cm. These data indicate that the amorphous film is more promising than the crystallized film as a gate insulator. The leakage current was comparable to previously reported results (Suzuki & Kato, 2007, 2009), but was smaller than that of a HfO$_2$ film deposited using atomic layer deposition (Chiou et al., 2007). At 700 °C, crystallization roughens the layer structure of the film as described in section 4.2 and provides a short leakage path through grain boundaries (Chiou et al., 2007, Zhu et al., 2002). The *I-V* characteristics for both forward and reverse biases in the Al/HfO$_2$/SiO$_2$/n-Si structure are unsymmetrical against bias voltages. This is probably because the potential barrier in the band diagram between the Al electrode and the HfO$_2$ film and that between the HfO$_2$ film and the SiO$_2$ film may differ between forward and reverse bias conditions. For the reverse bias condition, the energy slope of each band diagram of the Al/HfO$_2$/SiO$_2$/n-Si structure goes upwards and the difference between the work function of Al and the electron affinity of HfO$_2$ presumably creates a potential barrier against the flow of carriers. Therefore, the flow of electrons or holes may be suppressed by the barrier, resulting in

current lower than that in the forward bias condition in which a potential barrier may not exist.

The unsymmetrical *I-V* characteristics are true in the "HNO₃ sol" case. The smallest leakage current in the "HNO₃ sol" HfO₂ thin films was seen for the amorphous films fired at 450 ℃, which might be attributable to the smooth surface structure of the film. At 450 ℃, the H₂O in the HfO₂ thin film desorbed less compared with that in the amorphous film fired at 350 ℃. Therefore, there is some possibility for sol-gel-derived HfO₂ thin films to be used as alternative high-*k* materials for gate insulators in CMOS devices; however, the amount of H₂O should be reduced to a minimum (Ragnarsson et al., 2009).
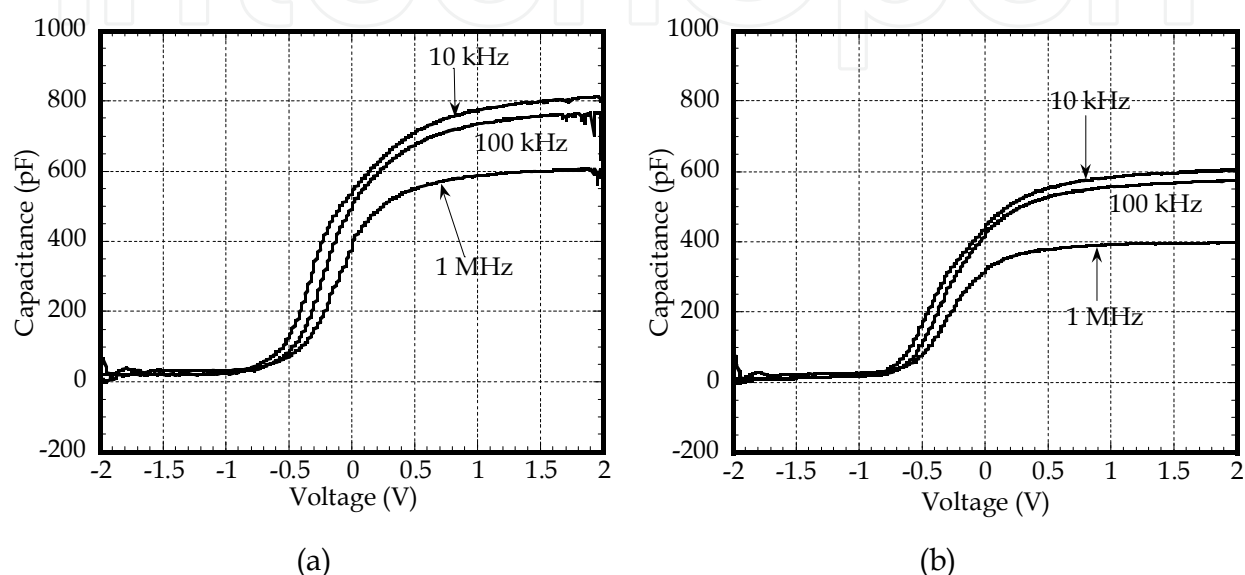

Fig. 20. *C-V* curves for Al/HfO₂/SiO₂/n-Si capacitors with HfO₂ films using
(a) "HCOOH sol" at a firing temperature of 550 ℃ and (b) "HNO₃ sol" at 450 ℃
(Shimizu et al., 2010).

The *C-V* curves for Al/HfO₂/SiO₂/n-Si capacitors were examined in relation to the "HCOOH sol" HfO₂ film fired at 550 ℃ and to the "HNO₃ sol" HfO₂ film fired at 450 ℃, respectively. The *C-V* curves are plotted in Figure 20 from – 2 to 2 V, representing the practical range for device operation. The *C-V* curves show a well-defined transition from depletion and inversion to accumulation as the applied voltage was varied from – 2 to 2 V, similar to the *C-V* curves for normal Al/SiO₂/Si capacitors (Nicollian & Brews, 1981). The *C-V* characteristics do not show any dependence on firing temperature, but the capacitance decreases with increasing frequency. On the basis of the well-defined capacitance in the plotting of a *C-V* curve at a frequency of 100 kHz, the relative permittivity ε_{HfO2} of the "HCOOH sol" HfO₂ film was calculated to be 11, with an effective oxide thickness (EOT) of 2.1 nm (HfO₂ film thickness: 7.4 nm). The SiO₂ film thickness was 2 nm, so the relative permittivity ε_{HfO2} was calibrated using that of SiO₂. The relative permittivity was much higher than that of silicon dioxide (SiO₂, 3.9), but is comparable to previously reported results (10~11) (Suzuki & Kato, 2009). The difference in the relative permittivity ε_{HfO2} between the sol-gel HfO₂ film and bulk HfO₂ may be due to the presence of the SiO₂ film and nanopores in the HfO₂ film.

For the "HNO₃ sol" HfO₂ film, the relative permittivity was calculated to be 11 and the EOT was 3.9 nm (HfO₂ film thickness: 10.9 nm). The "HCOOH sol" HfO₂ film is promising, but it

Characterization of Sol-Gel-Derived and Crystallized
HfO$_2$, ZrO$_2$, ZrO$_2$-Y$_2$O$_3$ Thin Films on Si(001) Wafers with High Dielectric Constant

335

requires a relatively higher permittivity and a smaller film thickness to achieve a reasonable EOT for highly integrated CMOS devices. For EOT scaling, the necessity of suppressing the liberation of H$_2$O from the HfO$_2$ film at Si oxidation temperatures has been emphasized (Ragnarsson et al., 2009).

The reported *C-V* curves in Fig. 20 show a small reduction with increasing frequency. The relative permittivity decreases with increasing growth temperature of the high-*k* film (ZrO$_2$) and frequency (Kukli et al., 2001, 2002). In general, the relative permittivity is essentially governed by the polarization of the material, and decreases with increasing frequency. In the present sol-gel-derived HfO$_2$ films, H$_2$O, OH groups in the nanopores, and other impurities probably caused electronic and ionic polarizations, thereby giving rise to the possibility of the frequency dependence of the capacitance. One possible way of refining the electrical performance of sol-gel-derived HfO$_2$ films is to use a firing environment of oxygen, inert gas, or forming gas. Thus, the amount of H$_2$O, defects, and impurities in sol-gel-derived HfO$_2$ films must be reduced to make the films applicable as a semiconductor gate insulator material.

7. Characterization of sol-gel-derived and crystalline ZrO$_2$ thin films on Si(001) wafers

7.1 Crystallinity of sol-gel-derived ZrO$_2$ thin films on Si(001) wafers

XRD patterns were obtained for sol-gel-derived ZrO$_2$ films on Si(001) wafers fired at 450, 550, and 700 °C for 30 min (Figure 21). For the ZrO$_2$ film fired at 450 °C, a halo-like pattern
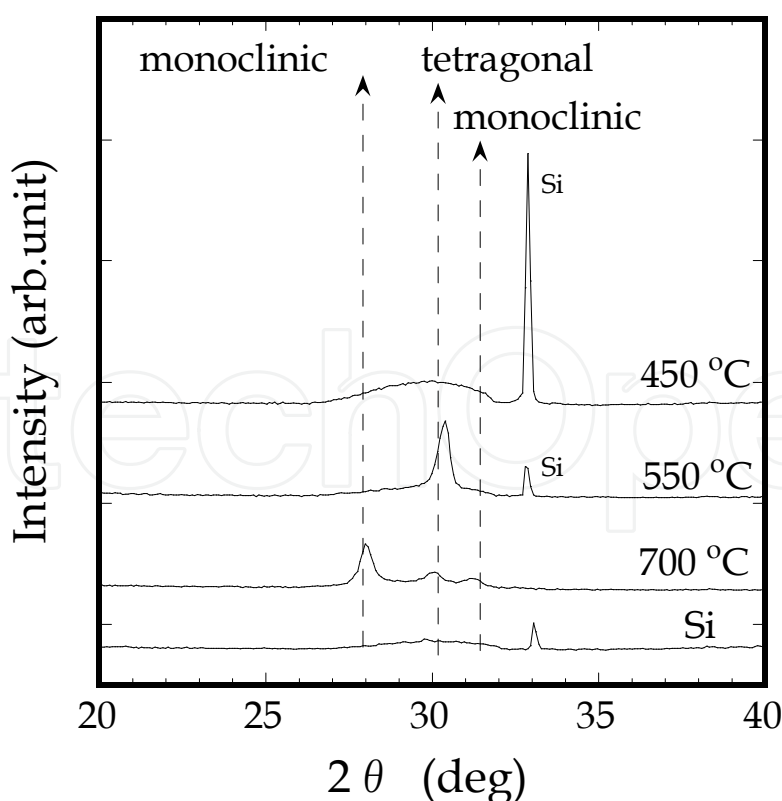

Fig. 21. XRD patterns obtained for ZrO$_2$ films on Si fired at 450, 550, and 700 °C for 30 min. The XRD pattern for the Si substrate is also shown for reference (Shimizu et al., 2009).

was observed at approximately $2\theta = 30°$, indicating that the film was still amorphous (Liu et al. 2002, Shimizu et al., 2009). The diffraction peak of 33° is ascribed to the Si (001) wafer. At 550 °C, a new peak appeared at $2\theta = 30.3°$, which was determined to be tetragonal (011) (JCPDS card, Liu et al., 2002, Shimizu et al., 2010), and the lattice interplanar distance was calculated to be 0.295 nm. In addition, at 700°C, three peaks at $2\theta = 28$, 30.3, and 31.3° were observed. The two peaks at $2\theta = 28$ and 31.3° were determined to be monoclinic (111) and monoclinic (111), respectively, because the calculated lattice interplanar distances were 0.319 and 0.286 nm, which correspond to the reported values of 0.316 and 0.284 nm. The ZrO_2 thin films fired at 700 °C consisted of a mixed crystal of tetragonal and monoclinic structures. Rapid temperature annealing (RTA) above 700 °C results in a mixture of monoclinic and tetragonal phases (Liu et al., 2002).

7.2 Spectral analyses of sol-gel-derived ZrO_2 thin films by TPD

Figure 22 shows the TPD curves of H_2O ($m/z = 18$) that evolved from the sol-gel-derived ZrO_2 thin films on Si, which were fired at 350, 450, 550, and 700 °C for 30 min. The vertical axis indicates the current value of QMS. The film thicknesses were determined to be 10.2, 9.9, 7.6, and 8.1 nm, respectively. The intensity of the TPD curves decreased as the firing temperature increased, indicating that the amount of H_2O was reduced in the ZrO_2 films on Si(001)wafers. Since the TPD curves were unsymmetrical against the heating temperature,
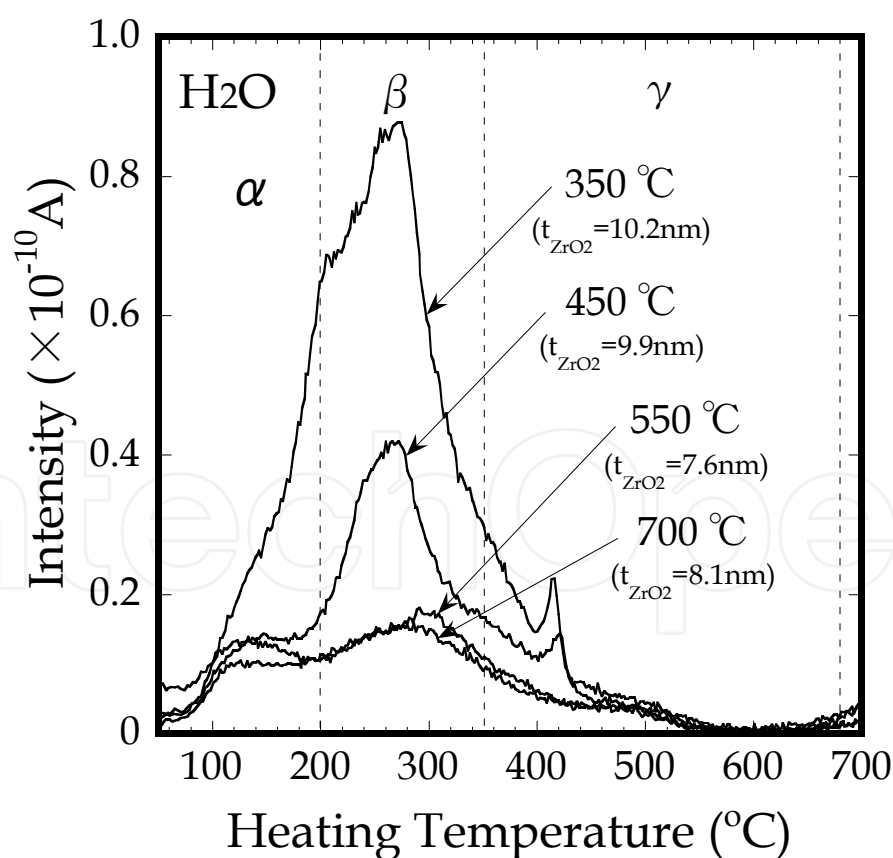

Fig. 22. TPD curves of H_2O ($m/z = 18$) that evolved from sol-gel-derived ZrO_2 thin films on Si fired at 350, 450, 550, and 700 °C for 30 min. The film thicknesses were 10.2, 9.9, 7.6, and 8.1 nm, respectively (Shimizu et al., 2009).

they were classified into three groups on the basis of the TPD results for SiO_2 formed by chemical vapor deposition (Hirashita et al., 1993): α, small peaks (small protrusions) between 100 and 200 °C; β, major peaks between 200 and 350 °C; and γ, small sharp peaks at approximately 410 °C for the samples fired at 350 and 450 °C. The measured TPD curve of H_2O had the main peak at a temperature of 260 °C with an unsymmetrical shape, providing evidence that several desorbed components were present during heating.

In a detailed analysis, the TPD curve for the sample fired at 350 °C was separated into five peak components using a Gaussian-type waveform (Figure 23). Component (a) is presumably due to physisorbed H_2O (mere adsorption of H_2O) on the surface of the ZrO_2 thin films. This was confirmed experimentally as discussed in the next subsection. Component (e) can be attributed to the desorption of H_2O through nanopores of the crystallized ZrO_2 thin film. Component (b) can be ascribed to the desorption of H_2O and/or chemisorbed Zr-OH bonds at the surface area. For components (c) and (d), H_2O desorption may have occurred because of the following reaction ($\equiv$ Zr-OH + HO-Zr $\equiv$ $\rightarrow$ $\equiv$ Zr-O-Zr $\equiv$ + H_2O).
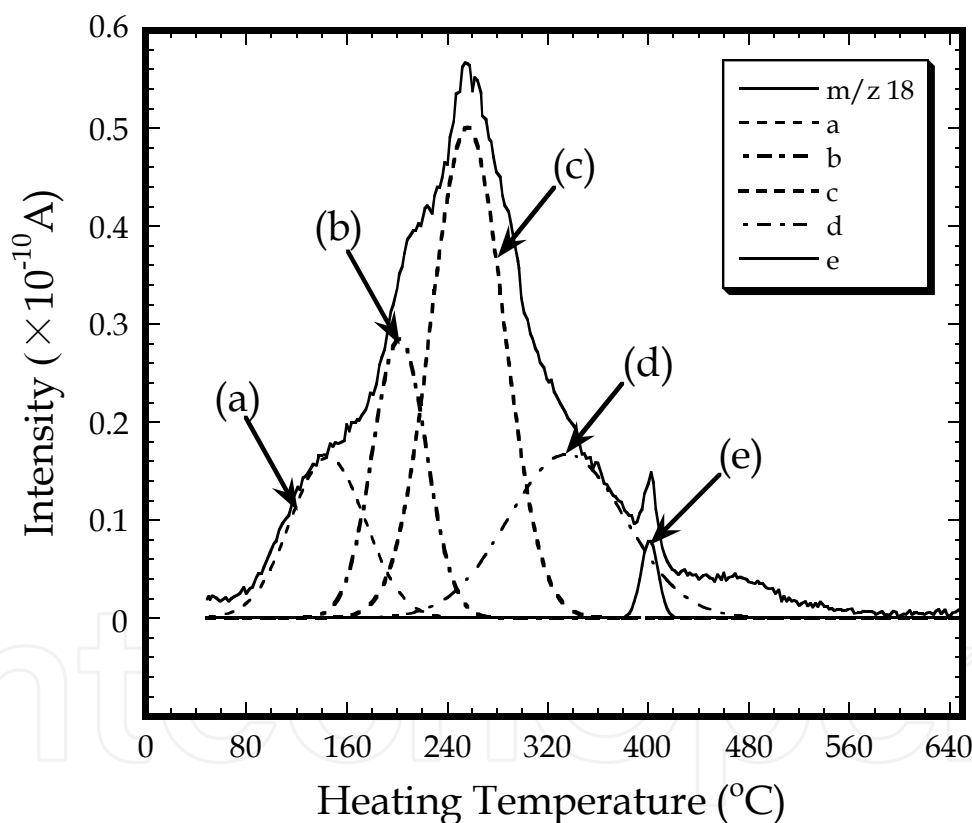

Fig. 23. TPD curve for the sol-gel-derived ZrO_2 thin film fired at 350 °C separated into five peak components using a Gaussian-type waveform as a function of the temperature measured with a thermocouple inside the TPD chamber (Shimizu et al., 2009).

7.3 Refractive indexes and film thicknesses of sol-gel-derived ZrO₂ thin films

The refractive indexes and film thicknesses were determined for sol-gel-derived ZrO_2 films fired at temperatures from 350 to 700 °C (Figure 24). The refractive indexes converged at 2.0, which is in good agreement with deposited ZrO_2 thin films (Moulder, 1995) and monoclinic
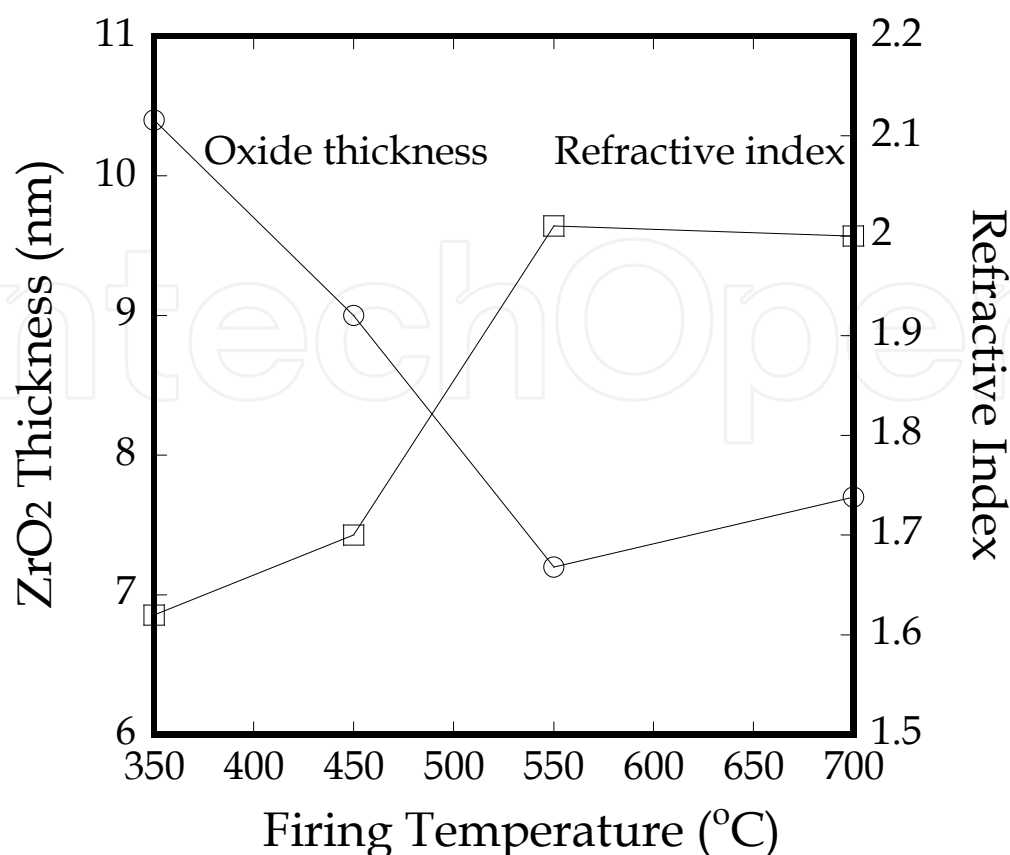
Fig. 24. Refractive indexes and film thicknesses of sol-gel derived ZrO_2 films at firing temperatures from 350 to 700 °C (Shimizu et al., 2009).

ZrO_2 crystals (Niinisto et al., 2004). The packing densities of the ZrO_2 films were calculated using the Lorentz-Lorentz equation (1) (Nishide et al., 2001). The refractive indexes were 1.62 at 350 °C, 1.70 at 450 °C, 2.01 at 550 °C, and 2.00 at 700 °C. The basic refractive index of the ZrO_2 crystal (monoclinic) for calculating the packing density was 2.22 (Yamada et al., 1988). Using this value, the packing densities were estimated to be 0.62 at 350 °C, 0.68 at 450 °C, 0.89 at 550 °C and 0.88 at 700 °C. The packing density of the films increased with increasing firing temperature. This is because more H_2O desorbed at higher firing temperatures and the small gaps of the nanopores were squeezed or evaporated.

7.4 Electrical characteristics of sol-gel-derived ZrO_2 films on Si(001) wafers

The *I-V* characteristics (current density vs electric field) were examined for sol-gel-derived ZrO_2 thin films on Si(001) wafers fired at 350, 450, 550, and 700 °C in air (Figure 25). For the sample fired at 550 °C, the leakage current was smaller than that of the amorphous ZrO_2 thin films fired at 350 and 450 °C. Leakage current deterioration was partially due to the considerable amount of H_2O in the film, but at 700 °C, crystallization was completed, and small surface cracks and surface relief observed with the AFM were responsible for the deterioration. The leakage current (forward bias) for the sample fired at 550 °C was approximately 4×10^{-3} A/cm² in an electric field of 1 M/cm, which is one or two orders of magnitude higher than that previously obtained (Chim et al., 2003). This difference is due to the densely compacted ZrO_2 thin film (Chim et al., 2003). For reverse bias, the leakage
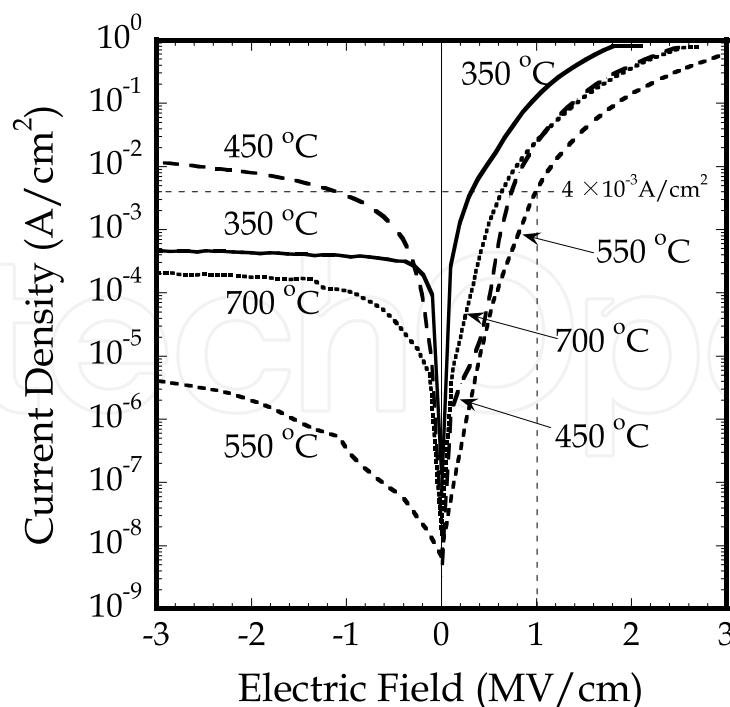
Characterization of Sol-Gel-Derived and Crystallized
HfO$_2$, ZrO$_2$, ZrO$_2$-Y$_2$O$_3$ Thin Films on Si(001) Wafers with High Dielectric Constant
339

Fig. 25. *I-V* characteristics (i.e., current density vs electric field relationship) for sol-gel-derived ZrO$_2$ thin films fired at 350, 450, 550, and 700 ºC in air. The reverse biases are plotted as absolute values (Shimizu et al., 2009).

current at 550 ºC was suppressed more than in the other films measured. Thus, there is some possibility for sol-gel-derived ZrO$_2$ thin films to be used as an alternative high-*k* material of gate insulators in densely packed CMOS devices.

To determine the relative permittivity ε_{ZrO2} of the sol-gel-derived ZrO$_2$ films, the *C-V* curves of the Al/ZrO$_2$/n-Si capacitors were obtained for the ZrO$_2$ thin film fired at 550 ºC for 30 min. The *C-V* curves are plotted in Figure 26 from – 2 to 2 V, representing the practical range for device operation. The *C-V* curves show a well-defined transition from depletion and inversion to accumulation as the applied voltage was varied from – 2 to 2 V, similar to the *C-V* characteristics of normal Al/SiO$_2$/Si capacitors (Nicollian & Brews, 1981). The *C-V* characteristics did not show any dependence on firing temperature, but the capacitance decreased with higher frequency. On the basis of the well-defined capacitances in the accumulation region of the *C-V* curves at a frequency of 100 kHz, the relative permittivity ε_{ZrO2} of the sol-gel-derived ZrO$_2$ film was calculated to be 12 and the EOT was 2.4 nm (ZrO$_2$ film thickness: 7.4 nm). The relative permittivity was higher than that of silicon dioxide (SiO$_2$; 3.9) and the EOT was comparable to previously reported results (~2.5 nm) (Chim et al., 2003). The relative permittivity of ZrO$_2$ formed by atomic layer deposition has been reported to be 23 (Niinisto et al., 2004). The *C-V* curves decline slightly with increasing frequency. The relative permittivity decreases with the growth temperature of ZrO$_2$ thin films and increasing frequency (Kukli et al., 2001). Relative permittivity is essentially governed by the polarization of the material, so it decreases as the frequency increases. In the sol-gel-derived ZrO$_2$ film, H$_2$O, OH groups in nanopores and other impurities probably induced electronic and ionic polarizations, so there is the possibility of the frequency dependence of capacitance. To refine the electrical performance of sol-gel-derived ZrO$_2$ films, an alternative firing environment such as
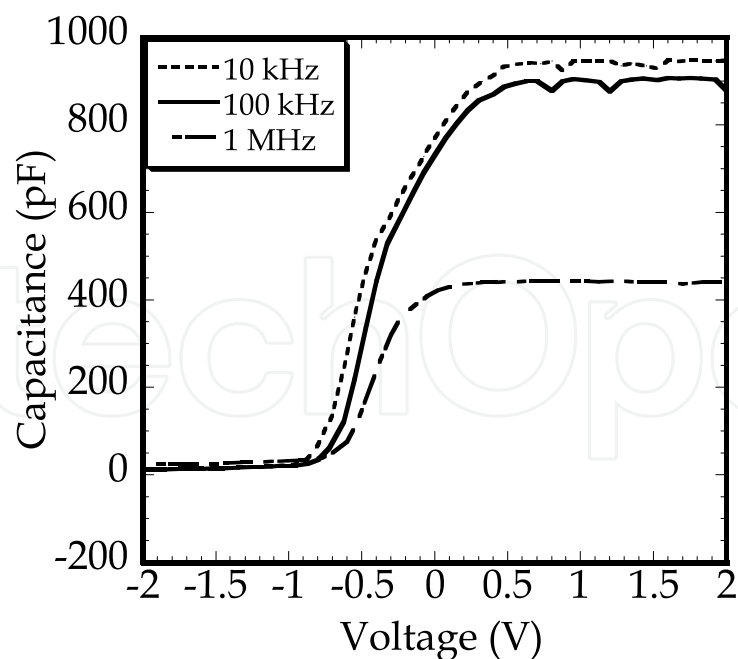
Fig. 26. *C-V* curves for Al/ZrO$_2$/n-Si capacitors, showing a well-defined transition from depletion and inversion to accumulation as a function of the applied voltage. The firing temperature of the ZrO$_2$ film was 550 °C for 30 min (Shimizu et al., 2009).

oxygen, inert gas, or forming gas must be used. Thus, there is some possibility for applying sol-gel-derived ZrO$_2$ thin films as a semiconductor gate insulator material. To fabricate improved ZrO$_2$ films, further experiments should be conducted to find an effective way of reducing impurities. Sol-gel-derived Y doped ZrO$_2$(ZrO$_2$-Y$_2$O$_3$) thin films on Si(001) wafers are also promising.

8. Characterization of sol-gel-derived crystalline ZrO$_2$ –Y$_2$O$_3$ thin films on Si(001) wafers

Sol-gel-derived Y doped ZrO$_2$ (ZrO$_2$-Y$_2$O$_3$) thin films on Si(001) wafers fired in air between 350 and 700 °C provide electrical characteristics, such as lower leakage current, in MOS capacitors superior to those of sol-gel-derived ZrO$_2$ thin films (Shimizu & Nishide, 2011). This is attributed to the reduced surface roughness of ZrO$_2$-Y$_2$O$_3$ thin films. The crystallized ZrO$_2$-Y$_2$O$_3$ surface fired at 700 °C clearly shows a crack-free state compared with ZrO$_2$ thin films. Thus, crystallized ZrO$_2$-Y$_2$O$_3$ thin films can reduce the leakage current, making them a promising material for gate insulators in aggressively scaled CMOS devices.

8.1 Film thicknesses and refractive indexes of sol-gel-derived ZrO$_2$-Y$_2$O$_3$

The film thicknesses and refractive indexes were measured for sol-gel-derived ZrO$_2$-Y$_2$O$_3$ films fired from 350 to 700 °C for 30 min (Figure 27). The film thickness tended to become thinner at temperatures higher than 450 °C (11 and 7 nm thick at 450 and 700 °C, respectively). If this ZrO$_2$-Y$_2$O$_3$ thin film has excellent characteristics with high permittivity, this thickness is suitable for a gate insulator material. Though the refractive indices between 350 and 700 °C increased with increasing firing temperature, the present results were lower than that reported for monoclinic ZrO$_2$ crystals (Niinisto et al., 2004).
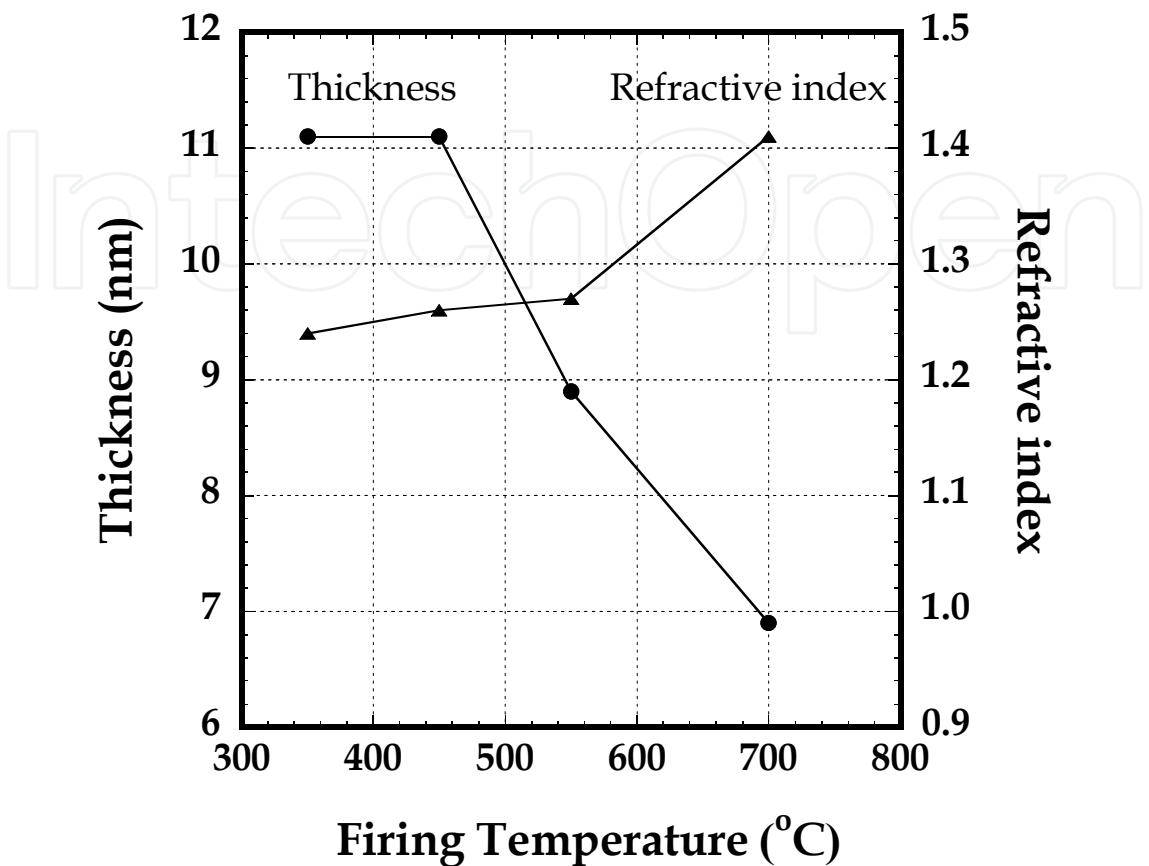
Characterization of Sol-Gel-Derived and Crystallized
HfO$_2$, ZrO$_2$, ZrO$_2$-Y$_2$O$_3$ Thin Films on Si(001) Wafers with High Dielectric Constant

341

Fig. 27. Film thicknesses and refractive indices of sol-gel-derived ZrO$_2$-Y$_2$O$_3$ films fired at 350, 450, 550 and 700 °C for 30 min (Shimizu & Nishide, 2011).

8.2 AFM-observed surface morphologies of sol-gel-derived ZrO$_2$-Y$_2$O$_3$ thin films

The surface microstructures of ZrO$_2$-Y$_2$O$_3$ thin films fired at 350 and 700 °C were observed with the AFM [Figs. 28(a) and 2(b)]. The morphology depended on the firing temperature. The surface of the ZrO$_2$-Y$_2$O$_3$ thin film fired at 350 °C showed a homogeneous structure [Fig. 28(a)]. The RMS surface roughness was 0.15 nm at 350 °C. The RMS value at 700 °C was 0.24 nm and the surface structure was slightly wavy, but it did not show grain boundaries and/or cracks caused by crystallization [Fig. 28(b)]. Similar results have been reported for crack-free nano- and microcrystalline ZrO$_2$-Y$_2$O$_3$ thin films deposited on sapphire substrates (Peters et al., 2009).

8.3 Electrical characteristics of sol-gel-derived ZrO$_2$-Y$_2$O$_3$ thin films on Si(001) wafers

The *I-V* characteristics (current density vs electric field) were investigated for sol-gel-derived ZrO$_2$-Y$_2$O$_3$ thin films fired at 350 and 700 °C in air, in comparison with those obtained for sol-gel-derived ZrO$_2$ thin films [Figure 29(a) and 29(b)]. The reverse bias
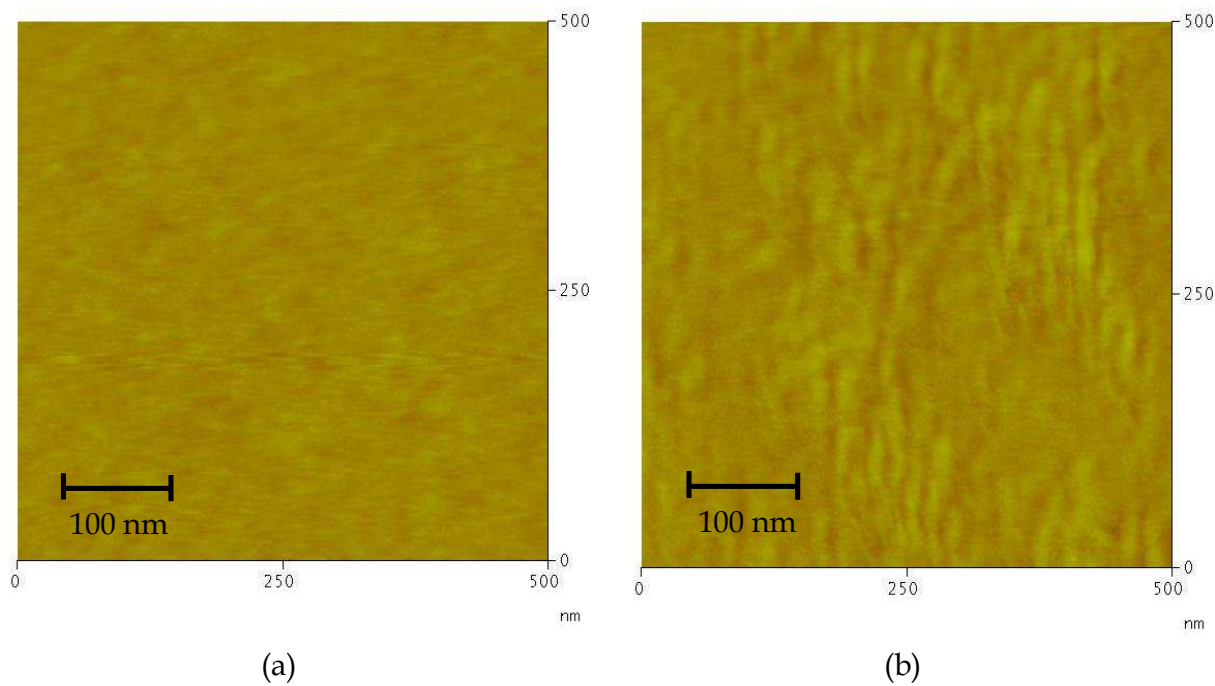
Fig. 28. AFM images of the surface microstructures of ZrO_2-Y_2O_3 thin films fired at
(a) 350 and (b) 700 ℃ (Shimizu & Nishide, 2011).
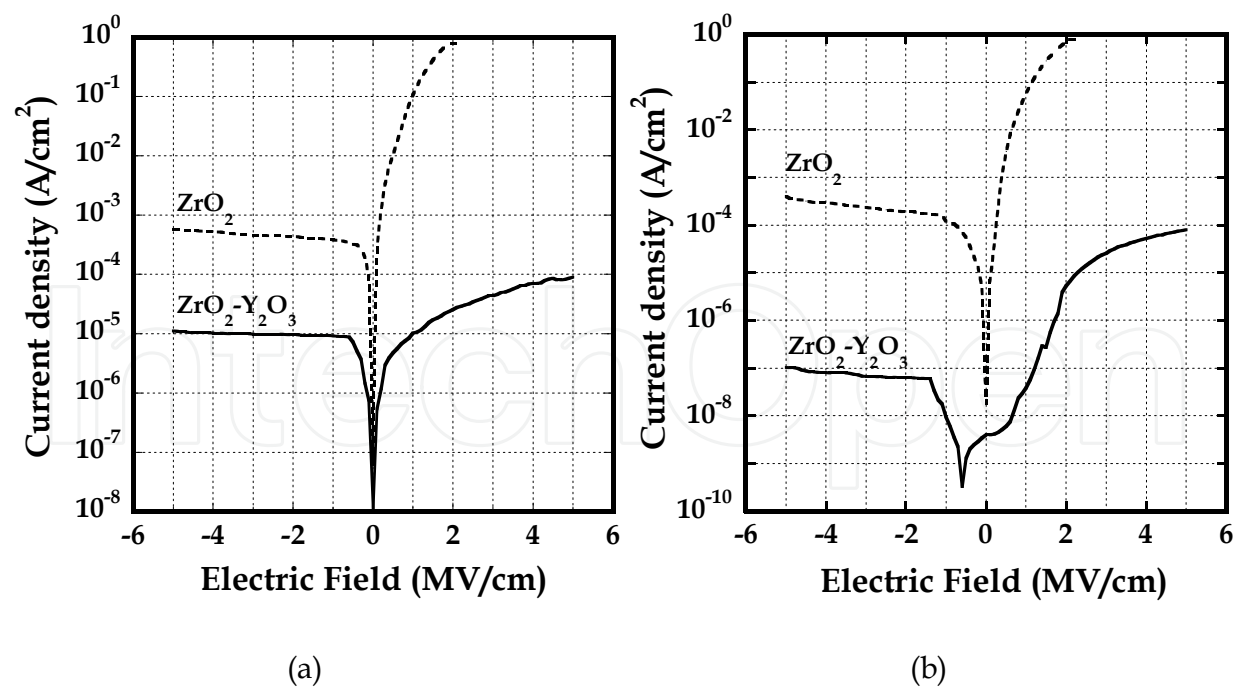

Fig. 29. *I-V* characteristics (i.e., current density vs electric field relationship) for sol-gel-
derived ZrO_2-Y_2O_3 thin films fired at (a) 350 and (b) 700 ℃ in air, respectively, in
comparison with those reported for sol-gel-derived ZrO_2 thin films
(Shimizu & Nishide, 2011).

Characterization of Sol-Gel-Derived and Crystallized
HfO$_2$, ZrO$_2$, ZrO$_2$-Y$_2$O$_3$ Thin Films on Si(001) Wafers with High Dielectric Constant

343

quantities are plotted as absolute values. The leakage current of the Al/ZrO$_2$-Y$_2$O$_3$/Si capacitors was approximately five orders of magnitude lower than that of the ZrO$_2$ thin films for forward bias at an electric field of 2 MV/cm and three orders of magnitude lower for reverse bias at -2 MV/cm, respectively (Shimizu & Nishide, 2011). This improvement of the leakage current is noteworthy. For the sample fired at 700 ºC, a similar reduction was observed for the Al/ZrO$_2$-Y$_2$O$_3$/Si capacitor. This is because the lower surface roughness and crack-free state of the ZrO$_2$-Y$_2$O$_3$ film surface may reduce the leakage current in comparison with the ZrO$_2$ thin films as described in subsection 5.4. For the ZrO$_2$-Y$_2$O$_3$ thin films fired between 350 and 700 ºC, the leakage current of the latter was two orders of magnitude smaller than that of the former [Fig. 29(b)]. This is probably due to the film quality caused by crystallization such as packing density and/or a considerable difference in the amount of H$_2$O in the film.

The leakage current (forward bias) for the sample fired at 700 ºC was approximately 5×10^{-7} A/cm^2 in an electric field of 1 M/cm (Shimizu & Nishide, 2011), which is one or two orders of magnitude lower than previously reported results (Chim et al., 2003). The latter results may be for densely compacted ZrO$_2$ thin films, because they were fabricated by sputtering in an argon-plus-oxygen gas ambient and annealed at 400 ºC in a nitrogen ambient for 5 min. For reverse bias, the leakage current at 700 ºC was superior to that of the other measured films. Therefore, there is some possibility for sol-gel-derived ZrO$_2$-Y$_2$O$_3$ thin films to be used as an alternative high-k material for gate insulators in miniaturized CMOS devices. However, the film quality must be improved further (Shimizu & Nishide 2011).

8.4 TPD analyses of sol-gel-derived ZrO$_2$-Y$_2$O$_3$ thin films

TPD was used to investigate the desorption of H$_2$O (m/z = 18) that evolved from sol-gel-derived ZrO$_2$-Y$_2$O$_3$ thin films on Si(001) wafers, which were fired at 350 and 700 °C for 30 min (Figure 30). The vertical axis indicates the current value of QMS. The film thicknesses were 11.1 and 6.9 nm, respectively. The intensity of the TPD curves decreased as the firing temperature increased, indicating that the amount of H$_2$O was reduced in the ZrO$_2$-Y$_2$O$_3$ thin films on Si(001) wafers. For the ZrO$_2$-Y$_2$O$_3$ thin film fired at 350 ºC, the peaks seen at 370 and 400 ºC are attributed to equipment noise.

Two TPD curves are close to those of ZrO$_2$ thin films (Shimizu & Nishide, 2011), except that the sample fired at 350 ºC does not show any similar protrusions between 100 and 200 ºC like those seen for the ZrO$_2$ thin film (Figure 22) (Shimizu et al., 2009). The peak was separated into several components using a Gaussian-type waveform (Figure 23), and the waveform indicated by the dashed line is shown as a function of temperature (Figure 30). The desorption temperature of the main peak of the ZrO$_2$-Y$_2$O$_3$ thin film was approximately between 100 and 200 ºC. This implies that the TPD peak may be due to physisorbed H$_2$O (mere adsorption of H$_2$O). In contrast, at 700 ºC, the TPD curves for H$_2$O desorption are similar in shape to that of the ZrO$_2$ thin film. The peak from 100 to 200 ºC is due to the adsorption of physisorbed H$_2$O and the main peak at approximately 250 ºC is caused by Zr-OH (chemisorbed) (Nishide et al., 2005, Takahashi & Nishide, 2004). The relative permittivity of ZrO$_2$ formed by atomic layer deposition has been reported to be 23 (Niinisto et al., 2004).
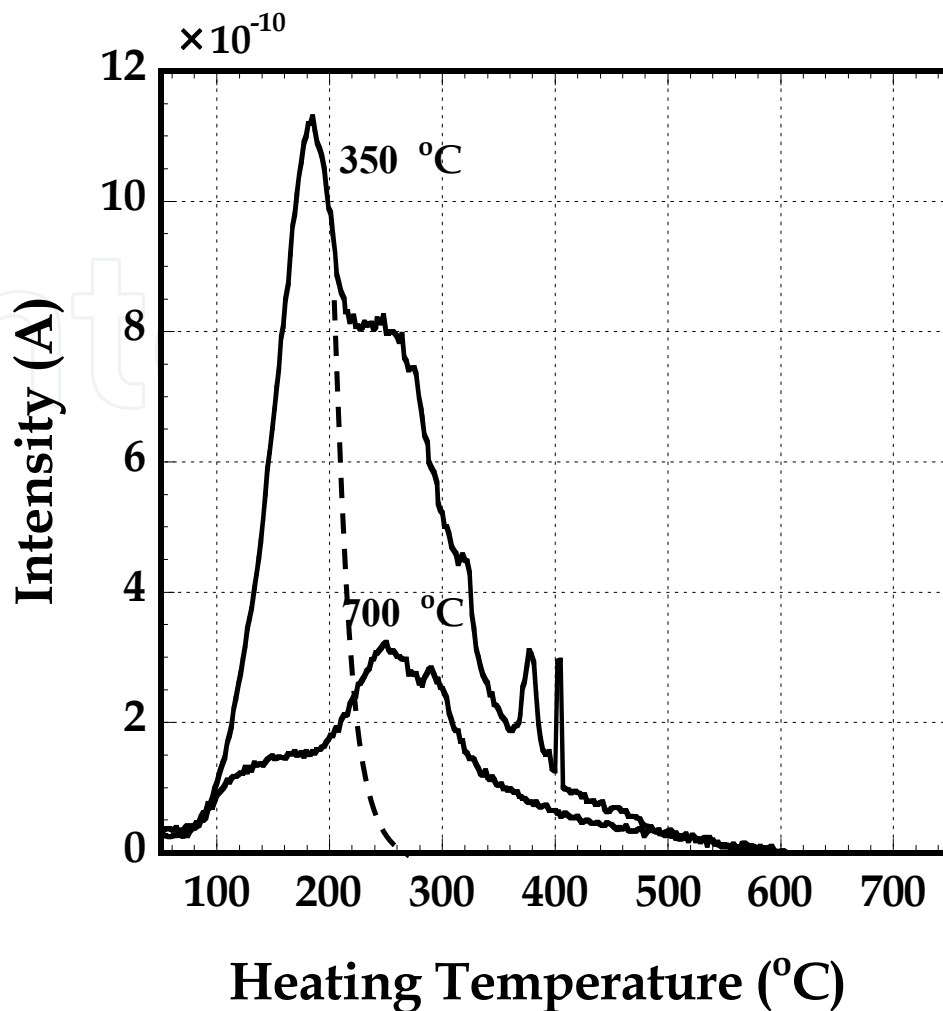
Fig. 30. TPD curves of H$_2$O (m/z = 18) that evolved from sol-gel-derived ZrO$_2$-Y$_2$O$_3$ thin films on Si(001) wafers, which were fired at (a) 350 and (b) 700 °C for 30 min (Shimizu & Nishide, 2011)

9. Conclusion

Sol-gel-derived HfO$_2$, ZrO$_2$ and Y doped ZrO$_2$(ZrO$_2$-Y$_2$O$_3$) thin films on Si(001) wafers fired in air between 350 and 700 °C were characterized physically, chemically and electrically with the aim of achieving alternative gate insulator materials for advanced CMOS devices. Crystallinity of the sol-gel-derived HfO$_2$, ZrO$_2$ films was found to be dependent on the firing temperature and sol solution. The relative permittivity of the films converged to that of bulk HfO$_2$ and ZrO$_2$ according to the specific sol solutions and firing temperatures. Residual H$_2$O and OH groups in the thin films were evaluated in reference to electrical characteristics such as the leakage current of MOS capacitors. The surface of the ZrO$_2$-Y$_2$O$_3$ thin films on Si(001) wafers showed less roughness than the HfO$_2$ and ZrO$_2$ thin films, resulting in lower leakage current in MOS capacitors. The leakage current of crystallized ZrO$_2$-Y$_2$O$_3$ thin films was shown to be lower than that of the amorphous state films because of the smooth crystalline surface of the latter in comparison with the ZrO$_2$ thin films. In conclusion, crystalline sol-gel-derived ZrO$_2$-Y$_2$O$_3$ thin films are postulated to be promising as alternative gate insulator materials of advanced CMOS devices.

Characterization of Sol-Gel-Derived and Crystallized
HfO$_2$, ZrO$_2$, ZrO$_2$-Y$_2$O$_3$ Thin Films on Si(001) Wafers with High Dielectric Constant

345

10. Acknowledgments

11. References

Blanchin, M. G., B. Canut, Y. Lambert, V. S. Teodorescu, A. Barau, & M. Zaharescu (2008) Structure and dielectric properties of HfO$_2$ films prepared by a sol-gel route, *Journal of Sol-Gel Science Technology*, 47, 165-172.

Chang, S. & R. Doong (2005) ZrO$_2$ thin films with controllable morphology and thickness by spin-coated sol-gel method, *Thin Solid Films*. 489, 17-22.

Chim, H., W. K., T. H. Ng, B. H. Koh, W. K Chol, J. X Zheng, C. H. Tung, & A. Y. Du (2003) Interfacial and bulk properties of zirconium dioxide as a gate dielectric in metal-insulator-semiconductor structures and current transport mechanism. *Journal of Applied Physics*, 93, 4788-4793.

Chiou, Y-K. C-H. Chang, C-C. Wang, K-y. Lee, T-B. Wu, R. Kwo, & M. Hong (2007) Effect of Al Incorporation in the Thermal Stability of Atomic-Layer-Deposited HfO$_2$ for Gate Dielectric Applications. *Journal of the Electrical Society*, 154, G99-G102.

Copel, M., E. Gibelyuk & E. Gusev (2000) Structure and stability of ultrathin zirconium oxide layers on Si(001). *Applied Physics Letters*, 76, 436-438.

Feldman, L. C., E. P. Gusev & E. Garfunkel: in *Fundamental Aspects of Ultrathin Dielectrics on Silicon Based Devices*, ed. E. Garfunkel, E. P. Gusev, and A. Vul (Kluwer, Dordrecht, 1998) p. 1.

Dey, S. K., C.-G. Wang, D. Tang, M. J. Kim, R. W. Carpenter, C. Werkhoven & W. Shero (2003) Atomic layer chemical vapor deposition of ZrO$_2$-based dielectric films: Nanostructure and nanochemistry. *Journal of Applied Physics*, 93, 4144-4157.

Gusev, E. 2005, *Defects in High-k Gate Dielectric Stacks*, Springer.

Feldman, L. C., E. P. Gusev, & E. Garfunkel: in *Fundamental Aspects of Ultrathin Dielectrics on Silicon Based Devices*, ed. E. Garfunkel, E. P. Gusev, and A. Vul (Kluwer, Dordrecht, 1998) p. 1.

Hirashita, N., S. Tokitoh, & H. Uchida (1993) Thermal Desorption and Infrared Studies of Plasm-Enhanced Chemical Vapor Deposited SiO$_2$ Films with Tetraethyiorthosilicate, *Japanese Journal of Applied Physics*, 32, 1787-1793 .

Huff, H. R. & D. C. Gilmer (2004) High Dielectric Constant Materials-VLSI MOSFET Applications, Springer, Berlin.

Joint Committee for Powder Diffraction Standards , JCPDS card No. 501089, No. 371484 (Joint Committee for Powder Diffraction Standards, Swarthmore, Pennsylvania).

Kozuka, H (2005) Handbook of Sol-Gel Science and Technology Processing, Characterization and Applications, Kluwer Academic Publishers, 1, 247-398.

Kukli, K., K. Forsgren, M. Ritala, M. Leskela, J. Ararik &A. Harsta (2002) Influence of growth temperature on properties of zirconium dioxide films grown by atomic layer deposition. *Journal of Applied Physics,* 95, 1833-1840.

Kukli, K., M. Ritala, J. Ararik, T. Uustare & M. Leskela (2002) Influence of growth temperature on properties of zirconium dioxide films grown by atomic layer deposition. *Journal of Applied Physics,* 95, 1833-1840.

Lee, M. S., C. H. An, J. H. Lim, J.H. Joo, H. J. Lee, & H. Kim (2010) Characteristics of Ce-Doped ZrO_2 Dielectric Films Prepared by a Solution Deposition Process, *Journal of Electrochemical Society,* 157, G142-G146.

Lucovsky, G. (2002) Correlation between electronic structure of transition metal atoms and performance of high-*k* gate dielectrics in advanced Si devices, *Journal of Non-Crystalline Solids* 303, 40-49.

Liu, W. C., D. Wu, A. D. Li, H. Q. Ling, Y. F. Tang, & N. B. Ming (2002) Annealing and doping effects on structure and optical properties of sol-gel-derived ZrO_2 thin films, *Applied Surface Science*, 191, 181-187.

Martinez, E., C. Leroux, N. Benedetto, C. Gaumer, M. Charbonnier, C. Licitra, C. Guedj, F. Fillot & S. Lhostis (2009) Electrical and Chemical Properties of the $HfO_2/SiO_2/Si$ Stack: Impact of HfO_2 Thickness and Thermal Budget. *Journal of Electrochemical Society* 156, G120-G124.

Moulder, J. F., W. F. Stickle, P. E. Sobol & K. D. Bomben (1995) *Handbook of X-ray Photoelectron Spectroscopy*, eds. J. Chastain & R. C. King (Physical Electronics, Minnesota,) 2nd ed., pp.44-45, 168-169.(HfO_2)

Moulder, J. F., W. F. Stickle, P. E. Sobol, & K. D. Bomben (1995) *Handbook of X-ray Photoelectron Spectroscopy*, eds. J. Chastain and R. C. King (Physical Electronics, Minnesota) 2nd ed., p. 44-45, p. 108-109.

Nicollian, E. H. & J. R. Brews: *MOS (Metal Oxide Semiconductor) Physics and Technology* (Wiley, New York, 1981) Chap.4, pp.99.

Niinisto, J., M. Putkonen, L. Niinisto, K. Kukli, M. Ritala, & M. Leskela (2004) Structural and dielectric properties of thin ZrO_2 films on silicon grown by atomic layer deposition from cyclopentadienyl precursor. *Journal of Applied Physics,* 95, 84-92.

Nishide, T., T. Tanaka, & T. Yabe (2004) Temperature programmed desorption analysis of sol-gel-derived titania films, *Journal of thermal analysis and calorimetry*. 90, 373-378.

Nishide, T. & M. Shibata (2001) Orientation and Surface Properties of Sol-Gel Derived Y_2O_3 Films. *Journal of Sol-Gel Science Technology*, 21, 189-193.

Nishide T., S. Honda, M. Matsuura, Y. Ito, & T. Takase (2000) Oriented and Non-Oriented HfO_2-Y_2O_3 Films on Amorphous Quartz Glass Substrates Prepared by Sol-Gel Processes. *Japanese Journal of Applied Physics*, 39, L237-L240.

Nishide, T., S. Honda, M. Matsuura, & M. Ide (2000) Surface, structural and optical properties of sol-gel derived HfO_2 films. *Thin Solid Films,* 371, 61-65.

Nishide, T., T. Yabe, N. Miyabayashi, & M. Sano (2004) Analysis of Firing Processes of Titania Gel Films Fabricated by Sol-Gel Processes. *Thin Solid Films,* 467 43-49.

Nishide, T., T. Meguro, S. Suzuki, & T. Yabe (2005) Ultraviolet Irradiation Hardening of Hafnia Films Prepared by Sol-Gel Processes, *Journal of Ceramic Society of Japan* 113 77-81.

Onili, Y., Y. Iwazaki, M. Hasumi, T. Ueno, & K. Kuroiwa (2009) HfO_2/Si and $HfSiO/Si$ Structures Fabricated by Oxidation of Metal Thin Films. *Japanese Journal of Applied Physics*, 48, 05DA01-1-05DA01-4.

Peters, C., A. Weber, B. Buts, D. Gerthsen, & E. I. Tiffee (2009) Grain-Size Effects in YSZ Thin-Film Electrolytes, *Journal of American Ceramics of Society*, 92, 2017-2024.

Parmentier, B., T. Conard, P. Roussel, S. D. Gendt, & M. M. Heyns (2009) The Importance of Moisture Control for EOT Scaling of Hf-Baced Dielectrics, *Journal of the Electrochemical Society*, 156, H416-H423.

Ragnarsson, L-A., D. P. Brunco, K. Yamamoto, Z. Tokei, G. Pourtois, A. Delabie, B.

Parmentier, T. Conard, P. Roussel, S. De Gendt, & M. M. Heyns (2009) *Journal of the Electrochemical Society*, 156, H416.

Robertson, J. & C. W. Chen (1999) Schottky barrier heights of tantalum oxide, barium strontium titanate, lead titanate, and strontium bismuth tantalite, *Applied Physics Letters*, 74, 1168-1170.

Robertson, J. (2000) Band offsets of wide-band-gap oxides and implications for future electronic devices, *Journal of Vacuum Science Technology*, B 18, 1785-1791.

Shimizu, H., K. Asayama, N. Kawai, & T. Nishide (2004) Material Microcharacterization of Sol-Gel Derived HfO₂ Thin Films on Silicon Wafers, *Japanese Journal Applied Physics*, 43, 6992-6993.

Shimizu, H., T. Sato, S. Konagai, M. Ikeda, T. Takahashi, & T. Nishide (2007) Temperature-Programmed Desorption Analyses of Sol-Gel Deposited and Crystallized HfO₂ Films. *Japanese Journal of Applied Physics*, 46, 4209-4214.

Shimizu, H., S. Konagai, M. Ikeda, & T. Nishide (2009) Characterization of Sol-Gel Derived and Crystallized ZrO₂ Thin Films. *Japanese Journal of Applied Physics*, 48, 101101-1-101101-6.

Shimizu, H., D. Nemoto, M. Ikeda, & T. Nishide (2010) Characterization of Sol-Gel Derived and Crystallized HfO₂ Thin Films Dependent on Sol Solution. *Japanese Journal of Applied Physics*, 49, 121502-1121502-6.

Suzuki, K. & K. Kato (2007) Effects of Modified Precursor Solution on Microstructure of (Y, Yb)MnO₃/HfO₂/Si, *Japan Society of Applied Physics*, 46, 6956-6959.

Suzuki, K. & K. Kato (2009) Characterization of high-*k* HfO₂ films prepared using chemically modified alkoxy-derived solutions, *Japanese Journal of Applied Physics*, 105, 061631-1-061631-3.

Takahashi, T. & T. Nishide (2004) Fabrication and Ultraviolet Irradiation Hardening of Sol-Gel-Derived Hafnia Films. *Journal of Ceramics Society of Japan*, 112 S234-S238.

Tonosaki, A., & T. Nishide (2010) Novel Petal Effect of Hafnia Films Prepared in an Aqueous Solution and Containing Hydroxy Acids. *Applied Physics Express*, 3, 125801-1-125801-3.

Wilk, G. D., R. M. Wallace & J. M. Anthony (2000) Hafnium and zirconium silicates for advanced gate dielectrics, *Journal of Applied Physics*, 87, 484-492.

Wilk, G. D., R. M. Wallace & J. M. Anthony (2001) High-*k* gate dielectrics: Current status and materials properties considerations, *Journal of Applied Physics*, 89, 5243-5275.

Yamada, T., M. Mizuno, T. Ishizuka, & T. Noguchi (1988) Liquidus-curve measurement in the system zirconia-hafnia, *Advanced Ceramics*, 24, 959-964.

Yang, X. M. Xl, X. F. (1996) Sintering behavior of (Y₂O₃-ZrO₂ gels). *Journal of Material Science*, 31, 2697-2703.

Yu, J. J., Q. Fang, J. Y. Zhang, Z. M. Wang & I. W. Boyd (2003) Hafnium oxide layers derived by photo-assisted sol-gel processing, *Applied. Surface Science*, 208-209, 676-681.

Zhan, Z. & H. C. Zeng (1999) A catalyst-free approach for sol-gel synthesis of highly mixed ZrO$_2$-SiO$_2$ oxide. *Journal of Non-Crystalline Solids*, 243, 26-38.

Zhu, W. J., T. Tamagawa, M. Gibson, T. Furukawa, & T. P. Ma (2002) Effect of Al Inclusion in HfO$_2$ on the Physical and. Electrical Properties of the Dielectrics, *IEEE Electron Device Letters*, 23, 649-651.
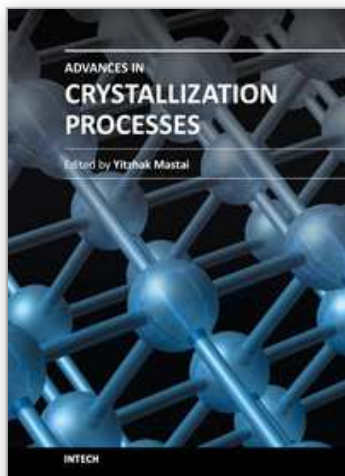
Advances in Crystallization Processes

Edited by Dr. Yitzhak Mastai

Crystallization is used at some stage in nearly all process industries as a method of production, purification or recovery of solid materials. In recent years, a number of new applications have also come to rely on crystallization processes such as the crystallization of nano and amorphous materials. The articles for this book have been contributed by the most respected researchers in this area and cover the frontier areas of research and developments in crystallization processes. Divided into five parts this book provides the latest research developments in many aspects of crystallization including: chiral crystallization, crystallization of nanomaterials and the crystallization of amorphous and glassy materials. This book is of interest to both fundamental research and also to practicing scientists and will prove invaluable to all chemical engineers and industrial chemists in the process industries as well as crystallization workers and students in industry and academia.

How to reference

In order to correctly reference this scholarly work, feel free to copy and paste the following:

Hirofumi Shimizu and Toshikazu Nishide (2012). Characterization of Sol-Gel-Derived and Crystallized HfO_2, ZrO_2, ZrO_2-Y_2O_3 Thin Films on Si(001) Wafers with High Dielectric Constant, Advances in Crystallization Processes, Dr. Yitzhak Mastai (Ed.), ISBN: 978-953-51-0581-7, InTech, Available from: http://www.intechopen.com/books/advances-in-crystallization-processes/characterization-of-sol-gel-derived-and-crystallized-hfo2-and-zro2-thin-films-with-high-dielectric-c

INTECH
open science | open minds